

THESIS FOR THE DEGREE OF LICENTIATE OF ENGINEERING

Numerical and Experimental Investigation of Hydrodynamic Mechanisms in Erosive Sheet Cavitation

MOHAMMAD HOSSEIN ARABNEJAD



Department of Mechanics and Maritime Sciences
CHALMERS UNIVERSITY OF TECHNOLOGY
Göteborg, Sweden 2018

Numerical and Experimental Investigation of Hydrodynamic Mechanisms in
Erosive Sheet Cavitation

MOHAMMAD HOSSEIN ARABNEJAD

© MOHAMMAD HOSSEIN ARABNEJAD, 2018

Report no 2018:19

Department of Mechanics and Maritime Sciences
Chalmers University of Technology
SE-412 96 Göteborg
Sweden
Telephone + 46 (0)31-772 1000

Printed by Chalmers Reproservice
Göteborg, Sweden 2018

Numerical and Experimental Investigation of Hydrodynamic Mechanisms in Erosive Sheet Cavitation

MOHAMMMAD HOSSEIN ARABNEJAD

Department of Mechanics and Maritime Sciences

Chalmers University of Technology

Abstract

Cavitation erosion is one of the limiting factors in the design of hydraulic machinery as it is associated with the reduction in the operating life-time of a hydraulic machine and a significant increase in maintenance cost. In order to be able to design a hydraulic machine with a low risk of cavitation erosion, understanding the hydrodynamic mechanisms controlling the cavitation erosion is of great importance. A precondition of these hydrodynamic mechanisms is the creation of a transient cavity that collapses violently as it travels into the high-pressure regions; this creation is often called the shedding of cavity structures. Therefore, understanding the shedding process of the cavity structures plays an important role in providing the knowledge related to hydrodynamic mechanisms of cavitation erosion.

In this thesis, the dynamics of cavitating flows over a NACA0009 foil are investigated using numerical and experimental methods. The shedding behavior of cavity structures is analyzed based on the results from the numerical simulations and high-speed videos. For erosion assessment, the location of erosive collapses in the cavitating flow is determined using a paint test method. These locations and the detectable collapse events in the high-speed videos are used to find the relation between the erosion patterns and cavitation dynamics. In order to numerically assess the areas with high risk of cavitation erosion, the cavitating flow is simulated using a compressible solver, capable of capturing the shock-waves upon the collapse of cavities. The areas with high risk of cavitation erosion, identified with the compressible solver, is compared with the results from paint test. The results from the compressible solver are used to investigate the hydrodynamic mechanisms of erosive collapses.

Keywords: Sheet cavitation, High speed visualization, Paint test, Numerical simulation, Shedding behavior, Hydrodynamics mechanisms of cavitation erosion

Acknowledgement

First and foremost, I would like to express my sincere gratitude to my supervisor Professor Rickard E. Bensow for his support, guidance, and patience. I am also grateful to my colleagues in Marine Technology Division, especially Dr. Abolfazl Asnaghi who helped me set up the simulations in OpenFOAM.

My sincere thanks goes to my friend, Mr. Ali Amini, for his help and participation in the experimental part of this thesis. I would like to thank Dr. Mohamed Farhat for hosting me during my visit to Laboratory for Hydraulic Machines at EPFL and for fruitful discussion we had about leading-edge cavitation.

This work is funded through the H2020 project CaFE, a Marie Skłodowska-Curie Action Innovative Training Network project, grant number 642536.

The simulations were performed on resources at Chalmers Centre for Computational Science and Engineering (C3SE) provided by the Swedish National Infrastructure for Computing (SNIC).

Last but not the least, I would like to thank my family, my parents and my sister for supporting me throughout my life.

CONTENTS

1	Introduction	1
1.1	Cavitation erosion	1
1.1.1	Shock-wave	2
1.1.2	Micro-jet	3
1.2	Hydrodynamic mechanism of cavitation erosion	3
1.3	Shedding of transient cavities	8
1.4	Numerical simulation of cavitating flows	10
1.5	Objectives and scope of this thesis	12
2	Methods	15
2.1	Modified NACA0009 foil case	15
2.1.1	Experimental set-up	15
2.1.2	Computational domain and boundary conditions	17
2.2	High speed observation and paint test	18
2.3	Numerical methods	18
2.3.1	Pressure-based incompressible solver with TEM cavitation model	18
2.3.2	Density-based compressible solver with equilibrium cavitation model	21
3	Results	29
3.1	Primary shedding	29
3.1.1	Secondary re-entrant jet	33
3.1.2	Delay in the formation of main re-entrant jet	35
3.1.3	Correlation between stream-wise pressure gradient at closure line and re-entrant jet	37
3.2	Secondary shedding	38
3.3	Erosion assessment using paint test	49

3.4	On the relationship between cavitating structures and erosion patterns	50
3.4.1	Collapse events in region 1	50
3.4.2	Collapse events in region 2	50
3.4.3	Collapse events in region 3	51
3.4.4	Collapse events in region 4	54
3.5	Erosion assessment using compressible solver	55
4	Conclusions	61
	REFERENCES	63

LIST OF FIGURES

1.1	a) Snapshots of a collapsing bubble(the collapse occurs at $t = 93\mu s$). b) Snapshots of collapse-induced shock-wave [1]	2
1.2	Pressure distribution around a collapsing bubble as a function of the distance from the center of the bubble. a) before collapse, b)after collapse.[2]	3
1.3	The evolution of bubble interface when the bubble collapse near the surface [3]	4
1.4	Hydrodynamic mechanisms controlling cavitation erosion by Bark et al. [4, 5, 6]	6
1.5	hydrodynamic mechanisms of erosion in the cavitating flow over a venturi by Dular and Petkovsek [7, 8]	7
1.6	Erosion pattern for a cavitating flow over NACA0015 foil by Van Rijsbergen et al. [9]	8
1.7	Erosion pattern for a cavitating flow over a twisted foil by Cao et al. [10]	8
1.8	Description of the creation mechanism of re-entrant jet by Callenaere et al. [11]	9
2.1	A schematic image of EPFL high speed cavitation tunnel	16
2.2	A schematic view of the experimental set-up and operating conditions	16
2.3	Computation configuration for the foil a) computation domain, b) definition of boundary conditions ,c-i) grid topology , c-ii) close view of grid spacing in the incompressible simulation, c-iii) close view of grid spacing in the compressible simulation	17
2.4	Foil coated with layer of stencil ink, a) status of ink layer before the cavitation test,b) thickness of the ink layer over dashed red line in (a)	19
2.5	Initial conditions and computational domain for 1D Cavitating flow	25

2.6	Comparison between the numerical solution and analytical solution[12] for a 1D cavitating flow	26
2.7	Simulation of a collapsing bubble a) computational domain and BCs for the collapsing bubble case, b) comparison of numerical simulation and solution of equation 2.32 for a collapsing bubble.	27
3.1	The variation of maximum length of sheet cavity and Strouhal number as function of cavitation number	29
3.2	Primary shedding in HSV and numerical simulation for the cavitating flow with $\sigma = 1.25$ (Flow is from right to left and the trailing edge is marked by dashed red line).	30
3.2	Primary shedding in HSV and numerical simulation for the cavitating flow with $\sigma = 1.25$ (Flow is from right to left and the trailing edge is marked by dashed red line).	31
3.2	Primary shedding in HSV and numerical simulation for the cavitating flow with $\sigma = 1.25$ (Flow is from right to left and the trailing edge is marked by dashed red line).	32
3.3	Complex shedding behavior due to the delay in the formation of re-entrant jet (Flow is from right to left).	33
3.4	Instants corresponding to the formation of secondary re-entrant jet	34
3.4	Instants corresponding to the formation of secondary re-entrant jet.	35
3.5	Delay in the formation of re-entrant jet 2	36
3.5	Delay in the formation of re-entrant jet 2	37
3.6	Stream-wise pressure gradient on the surface of the foil and the stream-wise velocity on a plane perpendicular to a) secondary re-entrant jet, b) re-entrant jet 2.	38
3.7	Detachment of vapour structures related to secondary shedding in HSV.	39
3.8	Detachment process of structure CS1 due to interaction between re-entrant jet and the closure line of the sheet cavity (Flow is from right to left).	41
3.9	Analysis of vorticity components and terms in transport equation of stream-wise vorticity on C-C plane in figure 3.8, a) contours of vorticity components b) contours of the terms in transport equation of stream-wise vorticity.	42
3.10	Detachment process of structure CS2 from the closure line of the sheet cavity due to the secondary re-entrant jet (Flow is from right to left).	44
3.11	Analysis of vorticity components and terms in transport equation of stream-wise vorticity on D-D plane in figure 3.10, a) contours of vorticity components, b) contours of the terms in transport equation of stream-wise vorticity.	45
3.12	Detachment process of structure CS3 from downstream end of the cloud (Flow is from right to left).	47

3.13	Analysis of vorticity components and terms in transport equation of stream-wise vorticity on E-E plane in figure 3.12, a) contours of vorticity components b) contours of the terms in transport equation of stream-wise vorticity.	48
3.14	The paint removal after 15 min of cavitation test for different cavitation numbers (l_{max} : maximum length of the sheet cavity, x : stream-wise position from the leading edge).	49
3.15	Collapse events in region 1 for different cavitation numbers (Flow is from top to bottom and the trailing edge is marked by a red dashed line).	50
3.16	Collapse of small cavitating vortices in the upstream part of the cloud (Flow is from top to bottom and the trailing edge is marked by a red dashed line).	51
3.17	Collapse of structures in downstream end of rolling cloud (Flow is from top to bottom and the trailing edge is marked by a red dashed line).	52
3.18	Collapse of large cavitating vortex in upstream part of the cloud (Flow is from top to bottom and the trailing edge is marked by a red dashed line).	53
3.19	Collapse of horse-shoe vortical structures detached from the closure line of the sheet cavity (Flow is from top to bottom and the trailing edge is marked by a red dashed line).	54
3.20	Collapse of the large scale cloud cavities close to the trailing edge of foil (Flow is from top to bottom and the trailing edge is marked by a red dashed line).	55
3.21	Comparison between primary shedding in HSV and compressible simulation results for the cavitating flow with $\sigma = 1.25$ (Flow is from right to left and the trailing edge is marked by a red dashed line).	56
3.22	Erosion assessment using compressible solver, a)Maximum recorded pressure on each face of the surface, b) spatial distribution of collapse points with pressure higher than 60 bar(each sphere represents a collapse point)(Flow is from top to bottom).	58
3.23	Instants when the collapse of structures related to the sheet cavity induces pressure pulse large than 60 bars on the surface (Flow is from right to left).	59
3.24	Instants when the collapse of structures related to the cloud cavity induces pressure pulse large than 60 bars on the surface (Flow is from right to left).	60

1

Introduction

Despite numerous research, cavitation is still a challenging and complex phenomenon in hydraulic applications such as ship propellers, diesel injectors, hydraulic machinery, etc. Hydrodynamic cavitation in these applications occurs when the pressure in the liquid flow drops below the vapour pressure due to flow acceleration [13]. This pressure drop results in the formation of vapour pockets, known as cavities, in the liquid flow. The generated cavities are usually transported to high-pressure regions by the bulk flow. Due to the difference between the inside pressure of these cavities and the environmental pressure, violent collapse of these cavities may occur which is responsible for several ramifications in hydraulic devices. One example of these ramifications is the cavitation induced erosion [14].

1.1 Cavitation erosion

Cavitation erosion is defined as the material loss due to the repeated collapse of cavities close to a surface. The collapse of cavities induces high mechanical load and stress level on the nearby surface that can exceed yield/fatigue stress of the material. This high mechanical load eventually leads to failure of the material, which can be observed as the material removal. Cavitation erosion is one of the limiting factors in the design of hydraulic machinery as it is associated with reduction in the operating life-time of a hydraulic machine and leads to a significant increase in the maintenance cost. Therefore, numerous studies have been devoted to investigating the possible damaging mechanisms of cavitation erosion. These studies investigated both micro-scale mechanisms and macro-scale hydrodynamic mechanisms of cavitation erosion. In micro-scale level, two mechanisms identified in the literature are shock-wave and micro jet [14].

1.1.1 Shock-wave

Many numerical and experimental studies have shown that a shock-wave is emitted after the collapse of spherical bubbles. Figure 1.1 shows the snapshot of a collapsing bubble and the propagation of a collapse-induced shock-wave obtained by Lee et al. [1]. From the snapshots of bubble dynamics, it can be seen that the collapse occurs at $t = 93\mu s$ and this collapse is followed by the formation of a shock-wave which can be seen in figure 1.1b.

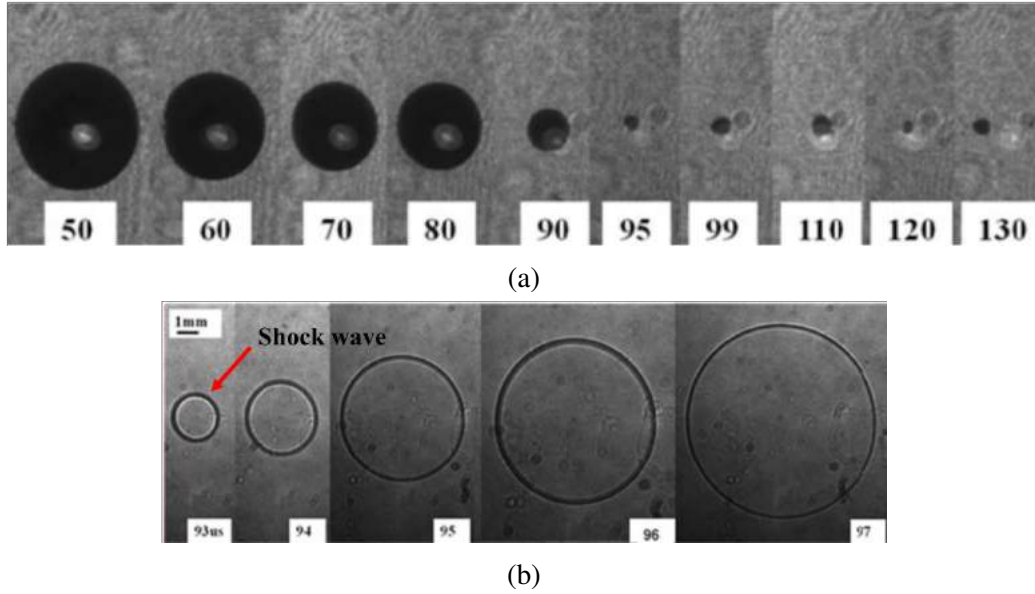


Figure 1.1: a) Snapshots of a collapsing bubble(the collapse occurs at $t = 93\mu s$).
b) Snapshots of collapse-induced shock-wave [1]

The formation of shock-waves can be also observed in the numerical and analytical analyses of spherical collapse of a bubble. The pressure distributions in the surrounding liquid of a collapsing bubble before and after the first rebound, obtained by Fujikawa and Akamatsu [2], is shown in figure 1.2. Before the collapse (figure 1.2a), the radial location of maximum pressure moves towards the bubble interface as the collapse proceeds and close to the end of collapse, the maximum pressure is located on the bubble interface. The pressure distribution after the collapse (figure 1.2b) shows the formation of a shock-wave after the collapse and the geometrical attenuation of this shock-wave as it propagates in the surrounding liquid. The mechanical load due to the interaction between the collapse induced shock-wave and nearby surface can lead to the deformation of the nearby surface. Fortes-Patella et al. [15] calculated this solid deformation numerically and showed that the calculated solid deformation matches well with the non-dimensional pit profile from the experimental pitting test. This observation confirms that shock-waves is a possible mechanism of cavitation erosion.

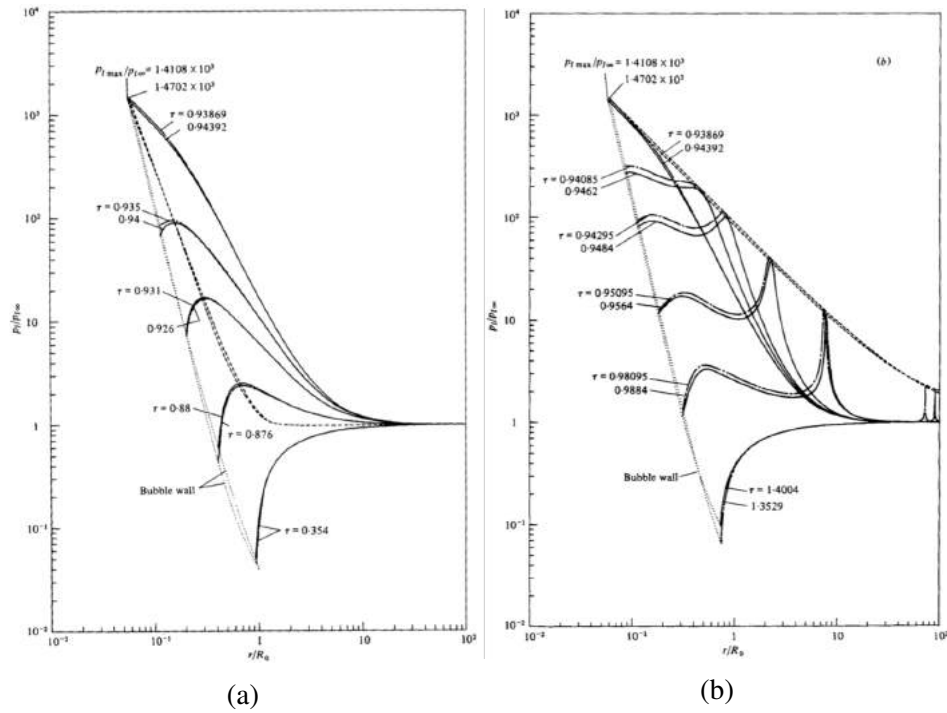


Figure 1.2: Pressure distribution around a collapsing bubble as a function of the distance from the center of the bubble. a) before collapse, b) after collapse.[2]

1.1.2 Micro-jet

Another mechanism of cavitation erosion is the microjet formation at the end of a non-spherical collapse of bubbles. When a bubble collapses near a surface, the collapse is not spherical due to the non-uniformity of the pressure field around the collapsing bubble [16, 17, 18, 19]. Figure 1.3 shows the collapse stage of an initially spherical bubble near the surface in the computation results by Plesset and Chapman [3]. As the collapse proceeds, the upper part of the interface bubble moves toward the wall, while the lower part of the interface becomes flat. The movement of the upper interface induces a jet-like flow in the surrounding liquid, called micro-jet, which pierces the bubble in the last stage of the collapse and impinges the wall. This impingement generates a water-hammer like pressure which can remove material from the surface in case of high pressure.

1.2 Hydrodynamic mechanism of cavitation erosion

The macro-scale hydrodynamic mechanism in which the collapse of a cavity becomes erosive or not is of great importance from the industrial point of view. The knowledge of these hydrodynamic mechanisms and their relationship with the design feature of a hydraulic machinery can become an input to the design process which produces designs with less risk of cavitation erosion. Due to this impor-

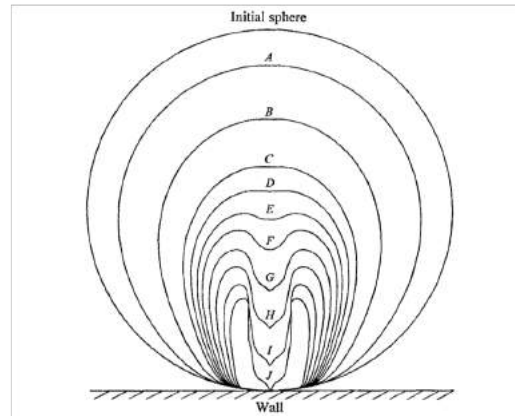


Figure 1.3: The evolution of bubble interface when the bubble collapse near the surface [3]

tance, several studies have been devoted to identifying large-scale hydrodynamic mechanisms of cavitation erosion. In this section, a collection of these studies have been reviewed.

In several publications, Bark et al. [4, 5, 6] outline different hydrodynamic mechanisms that influence the erosiveness of a collapsing cavity. A set of analysis models for the hydrodynamic mechanisms were established using kinematic analysis of cavity dynamics in high-speed videos and the erosion pattern obtained from the paint test. These analyses models are developed based on the concept of energy cascade which assumes an energy transfer between macro-scale cavities and small-scale cavities collapsing near the surface during an erosive collapse of a macro-scale cavity. The process of this energy transfer is denoted as focusing of a cavity. The following hydrodynamic mechanisms in which the focusing of a cavity can occur, are identified.

- Direct creation of a traveling cavity: A cavity with moving detachment point can be directly created in cavitating flows. One example of this cavity type is a traveling bubble which is shown in figure 1.4a.
- Shedding of a part of an attached or traveling cavity: Cavities can be detached from sheet or cloud cavities due to re-entrant flows. This process is shown in figure 1.4b.
- Upstream or local desinence of an initially attached cavity: The upstream condition of a cavitating flow can be changed for different reasons. One example is the change in the effective angle of attack in the cavitating flow over a propeller as it passes through the wake of a hull. A simplified model of this phenomena is the cavitating flows over an oscillating foil which is shown in figure 1.4c.
- Upstream moving collapse of an attached cavity: The downstream end of

an attached sheet cavity collapses toward the upstream attachment point. In this case, the primary collapse of the sheet cavity and the collapse of cavities created at the trailing edge of the sheet cavity can be erosive. An example of this process is shown in figure 1.4d.

- Generation of secondary cavities, typically from shear flow: An example of this mechanism, shown in figure 1.4e, is the creation of the cavities in the shear layer between the upstream moving re-entrant flow and the bulk flow.

The condition determining whether the generated cavities become erosive or not are further detailed in Bark and Bensow [6].

Dular and Petkovsek [7, 8] studied the hydrodynamic mechanisms of erosion in the cavitating flow over a venturi. They attached a thin layer of aluminium on the cavitating part of the venturi. Due to the softness of the aluminum layer, pitting can occur on this layer in a short period of time. The cavitation dynamics and status of the aluminium layer were recorded simultaneously by three cameras. Comparing the videos of cavitation dynamics and the pitting locations, Dular and Petkovsek were able to identify the following five mechanisms, shown in figure 1.5, that lead to the formation of pits on the aluminum layer.

- Spherical collapse of the cloud cavity: The spherical cloud is detached from the sheet cavity due to re-entrant jets. This cloud travels downstream where the pressure is above the vapour pressure. Due to this high pressure, the spherical cloud collapses violently and some pits were observed in the collapse location. The process for this mechanism is shown through the images A, B, C, D, E, F, G, and H in figure 1.5.
- Collapse of horse-shoe vortex: The cavitating vortex with the shape of horse-shoe is detached from the closure line of the sheet cavity. Pitting on the soft material was observed when the cavitating horse-shoe vortex starts to break up. The pits are located in the region where the legs of horse-shoe vortex are in contact with the surface. Images A, B, C, D, E, F, G, and H in figure 1.5 show the process of this mechanism.
- Collapse of twister vortex: The detachment process of twister cavitating vortex is the same as the detachment process of horse-shoe cavitating vortex. Vortices are created in the break-up region of the sheet cavity. In this case, the created vortices are not cavitating in their whole circumference and they contain mostly liquid. As these vortices travel downstream, they interact with the shed cloud and they start to cavitate. The break-up of these cavitating vortices causes pitting on the surface where the legs of the vortices are attached to the surface. Images M, N, and O in figure 1.5 represent this mechanism.
- Collapse of micro-bubbles at the closure of the sheet cavity: At the closure line of the sheet cavity, the pressure is high due to the existence of the

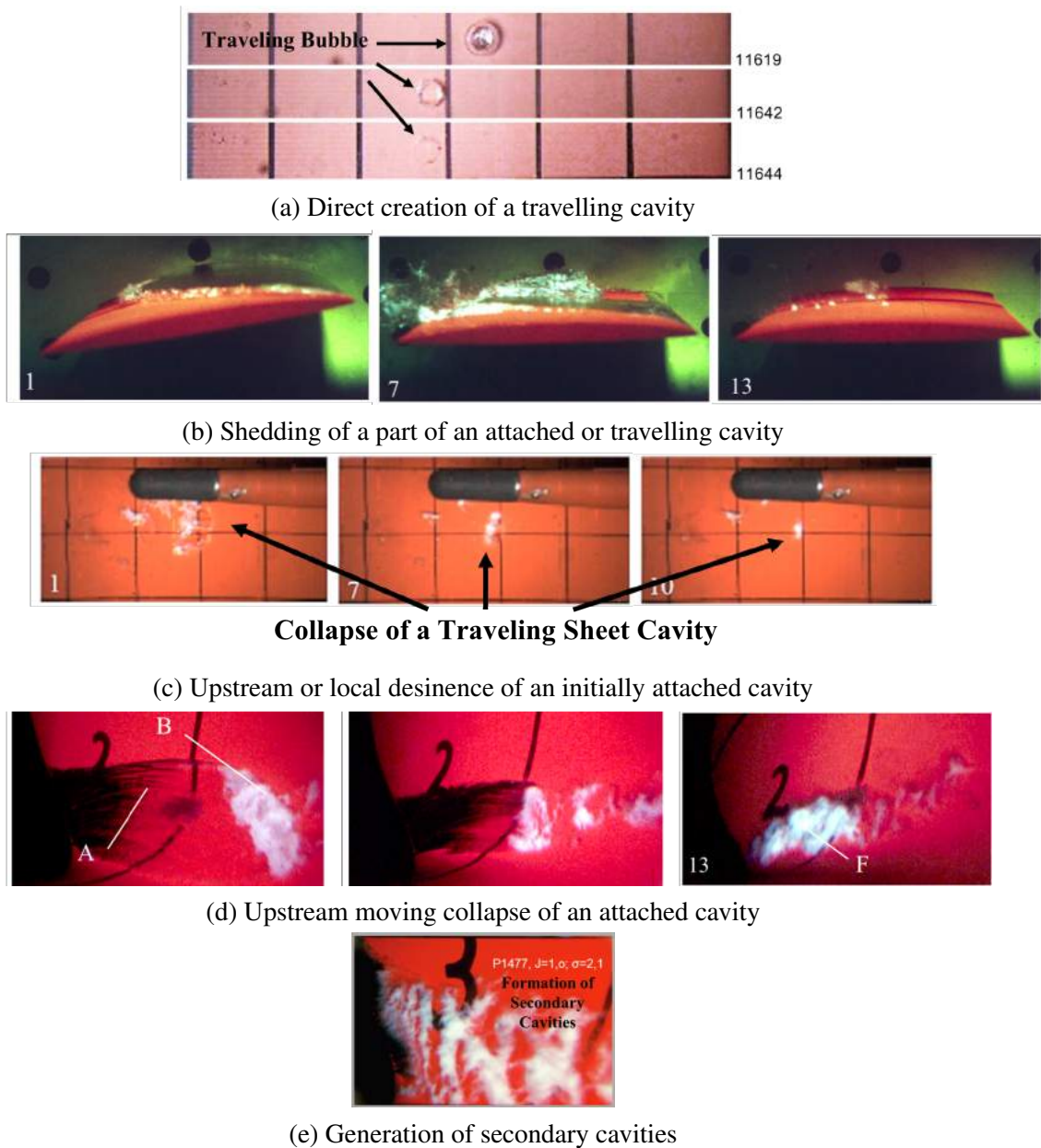


Figure 1.4: Hydrodynamic mechanisms controlling cavitation erosion by Bark et al. [4, 5, 6]

stagnation point. Micro-bubbles can be transported by the flow to this high-pressure region and collapse violently. If the collapse locations are near the surface, pitting of the surface can be expected. This mechanism is shown in images A, B, and C in figure 1.5.

- Collapse of micro-cavities at the break-up region of the cloud cavity: When the re-entrant jet moves upstream, it loses its momentum and this makes the re-entrant jet travels upward and interacts with the interface of the sheet

cavity. This interaction leads to the detachment of the cloud. In the break-up region, a local pressure increase can be expected. The collapse of micro-bubbles in this high-pressure region can create pits on the surface. Images A, B, C, and D in figure 1.5 represent this process.

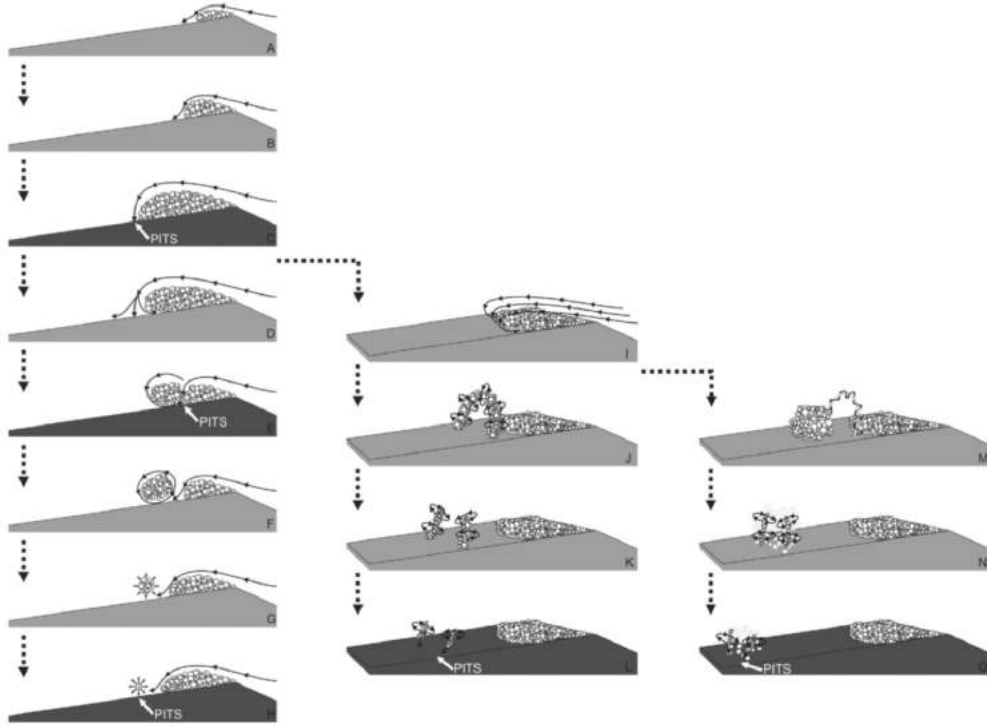


Figure 1.5: hydrodynamic mechanisms of erosion in the cavitating flow over a venturi by Dular and Petkovsek [7, 8]

Van Rijsbergen et al. [9] used high-speed visualization, paint test, and acoustic measurement to investigate the behavior of the cavitating flow over NACA0015 foil with the aim to identify the role of different cavitating structures in cavitation erosion. Figure 1.6 shows the status of the paint layer after one hour of cavitation test. Most of the paint removal occurred at the second half of the foil close to the trailing edge (TE). The analyses of high-speed videos and acoustic measurements showed that the paint removal is due to the collapse of small vapour structures in the shed cloud.

Cao et al. [10] investigated the relationship between cavitation structures and erosion damage on a twisted foil using high-speed visualization and paint test. Figure 1.7 shows the paint removal pattern in Cao et al.'s study obtained after 3 hours of cavitation test. Two regions of paint removal can be observed. Region 1 with severe paint removal is located around the rear part of the sheet cavity. In this location, high-speed videos showed that the unsteadiness of the sheet cavity leads to the detachment and the collapse of vapour structures. Figure 1.7 also shows

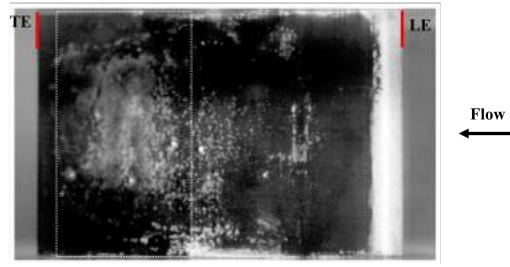


Figure 1.6: Erosion pattern for a cavitating flow over NACA0015 foil by Van Rijsbergen et al. [9]

that a region with moderate paint removal is located close to the TE of the twisted foil. This region corresponds to the collapse of the large horse-shoe cavitating structures.

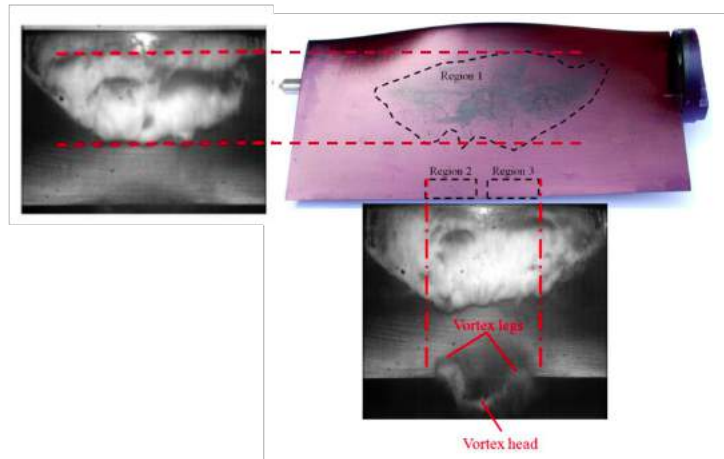


Figure 1.7: Erosion pattern for a cavitating flow over a twisted foil by Cao et al. [10]

1.3 Shedding of transient cavities

The majority of the hydrodynamic mechanisms of cavitation erosion reviewed in the previous sections involve the shedding of a transient cavity that collapses violently as it travels into the high-pressure regions. Two mechanisms of shedding of transient cavities have been observed in the literature, re-entrant jet and condensation shock-wave. In this section, these two mechanisms are described.

Numerous numerical simulation and experimental investigations showed the existence of a reverse flow at the closure line of the sheet cavity. This reverse flow is often called re-entrant jet in the literature. Callenaere et al. [11] provided a description, shown in figure 1.8, on how this re-entrant jet is created. At the

closure line, the flow slightly above the interface of the sheet cavity impinges on the surface and this creates a stagnation point at the closure line. The flow around this stagnation point is split into two streams, one traveling upstream and one traveling downstream. The upstream traveling flow is called re-entrant jet. According to the experimental study of de Lange and de Bruin [20], the effect of re-entrant flow on the sheet cavity depends on the thickness of the sheet cavity. Based on the cavity thickness, de Lange and de Bruin [20] identified two types of cavity shedding in the cavitating flows over hydrofoils, regular shedding and irregular shedding. In irregular shedding, the sheet cavity is thin and a weak re-entrant jet is created. The weak re-entrant jet does not have enough momentum to reach the leading edge and cuts the interface of the sheet cavity at varying locations downstream of the leading edge. This leads to the shedding of small vapour structures from the downstream end of the sheet cavity. In the case of thick sheet cavities, the re-entrant jet does not disturb the interface of the sheet cavity until it reaches the leading edge of the sheet where the re-entrant jet cuts off the sheet. This leads to the quasi-periodic detachment of a large scale cloud cavity. Foeth et al. [21] studied the shedding behavior of a cavitating flow over a twisted foil using high-speed videos. They found that the direction of a re-entrant jet is controlled by the shape of the sheet cavity. In the region where the closure line of the sheet cavity is convex, a converging re-entrant jet is created. The interaction of the converging re-entrant jet with the sheet cavity interface can cause the local shedding of small vapour structures.

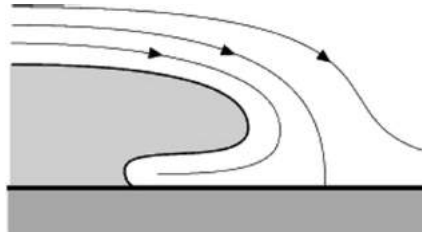


Figure 1.8: Description of the creation mechanism of re-entrant jet by Calenaere et al. [11]

The second mechanism for creation of a traveling cavity is the condensation shock-wave. The occurrence of the shock-wave at the closure line of an attached cavity was suggested by Jakobsen [22] in 1964. However, this phenomenon has been recently observed and investigated by Ganesh et al. [23]. These authors examined the dynamics of cavitating flow formed at the apex of a wedge geometry using X-ray densitometry and high-speed visualization. By measuring the instantaneous void-fraction field, they were able to observe an upstream traveling condensation shock-wave in the cavity attached to the apex of the wedge. When this shock-wave reaches the wedge apex, a large scale cloud cavity is pinched off. Ganesh et al. [23] also showed that the upstream and downstream condition of this shock-wave qualitatively satisfies simple one-dimensional bubbly shock relations.

1.4 Numerical simulation of cavitating flows

With the progress in the numerical modeling of cavitating flows, high-end numerical simulations have become a useful tool to study the main features of cavitating flows. Numerical simulations provide a complete access to the flow field that can be used to analyze the development of cavitating structures. The most common approach for simulating the cavitating flow in industrial applications is Reynolds-Averaged Navier Stokes (RANS) approach coupled with homogeneous mixture cavitation models. Several numerical studies have successfully applied this approach to study the averaged properties of cavitating flows. However, when the unsteady development of cavitating structures is of interest, a RANS approach fails to provide enough information to study this development. Furthermore, Coutier-Delgosha et al. [24] have shown that a RANS approach requires an ad-hoc modification to be able to predict the large-scale shedding of the cavitation structures. An alternative approach is Large Eddy Simulation (LES) which has been used to study the development of cavitating structures. Bensow and Bark [25] used this approach to simulate a cavitating flow over a propeller. By comparing the simulation results with experimental observation, they concluded that LES approach is capable of reproducing the most important mechanisms of cavitation, such as re-entrant jets and the upstream desinence of sheet cavity. Huuva [26] studied the cavitating flow over the twisted foil, which was examined experimentally by Foeth et al. [21], using a Large Eddy Simulation approach. Similar to the experiment, two types of shedding mechanisms were identified, the shedding of small cavitating structures from the sheet cavity closure-line due to side-re-entrant jet and the shedding of large-scale cavitating structures due to main re-entrant jet. The same geometry and flow condition was also investigated by Long et al. [27]. These authors analyzed the formation of cavitating structures using Eulerian and Lagrangian methods and showed that the stream-wise component of re-entrant flow becomes intensified when the re-entrant jet and side-entrant jet collide. The intensified re-entrant jet reaches the leading edge and breaks off the cloud cavity. They also showed that the remaining part of the sheet cavity after cloud pinch-off exhibits the shedding of small structures, similar to the observation made by Foeth et al. [21]. Dittakavi et al. [28] used an LES approach to study the formation of hair-pin vortical structures in the cavitating flow over a venturi. They showed that the collapse of vapour structures at the end of the sheet cavity is responsible for the formation of these hair-pin vortical structures. The analysis of the terms in the vorticity transport equation revealed that the presence of cavitation suppresses the vortex stretching terms in the inception region while the baroclinic term is intensified in the collapse region of cavitating structures. Huang et al. [29] and Ji et al. [30] used an LES approach to study the shedding dynamics in the cavitating flow over a foil. Their numerical results demonstrated a strong correlation between shedding dynamics and evolution of vortical structures. They also found that dilatation and vortex stretching terms are responsible for transforming the almost 2D cloud structures to 3D complex cavitating structures as these structures

move downstream. Lu et al. [31] performed LES of cavitating flows on two highly skewed propellers with slightly different designs. By analyzing the flow details captured by the LES, they were able to explain the impact of the difference in the design feature on the resultant cavitation behavior over these two propellers. Asnaghi and Bensow [32] studied the impact of mesh resolution in LES on capturing the shedding behavior of the cavitating flow over a twisted foil. Their investigation highlights that the small-scale shedding behavior can be captured if the mesh resolution is fine enough to capture the correct transportation of vortical structures. Gavaises et al. [33] used high-speed visualization and an LES approach to study the formation of unsteady sheet and cloud cavitation in an axis-symmetric nozzle. Their experimental and numerical results revealed the formation of cavitating vortex-filaments downstream of the sheet cavity inception point. These cavitating vortices are transported downstream by the flow where the higher surrounding pressure leads to the collapse of these cavitating vortices.

Numerical simulations have been used to estimate the aggressiveness of cavitating flows. These numerical simulations can be divided into two groups, numerical simulation based on an incompressible solver or a compressible solver. In the erosion assessment using incompressible methods, the aim is to model the aggressiveness of the flow based on the flow properties. Van et al. [34] reviewed several of these erosion models. Li et al. [35] proposed an erosion indicator based on the accumulation of the time derivative of pressure on the surface. The method was applied to a cavitating flow over a foil and an erosion pattern similar to the paint test results was obtained. However, the predicted erosion pattern was highly dependent on the threshold of the method. Fortes-Patella et al. [36] developed an erosion model which considers an energy balance between the potential energy of the collapsing cavity and the erosion damage. Although the predicted erosion pattern was in agreement with the experimental pitting test, the accuracy of the predicted erosion pattern depended on the conversion ratio between the potential energy of collapsing cavities and material damage [37]. Ochiai et al. [38] used acoustic pressure emitted from the microscopic bubble to predict cavitation erosion. As this method requires tracking of thousands of microscopic bubbles, it is computationally expensive and was applied to a 2D geometry. Koukouvini et al. [39] developed an erosion indicator based on the total derivative of pressure and vapour fraction. They applied this erosion indicator for the cavitating flow in the experiment of Franc et al. [40]. By comparing the predicted erosion pattern with the eroded areas in the experiment, they concluded that the developed erosion indicator is capable of identifying the areas with high risk of cavitation erosion qualitatively. Eskilsson and Bensow [41] compared the performance of three different erosion indicators developed for incompressible simulations. They compared the predicted erosion pattern with the paint test results and showed that none of the three models were able to predict the erosion pattern and further research on erosion indicator based on the incompressible simulation is needed. In addition to erosion models in incompressible simulations, compressible simulations have been used to study erosiveness of cavitating flows. As these simulations are ca-

pable of resolving shock-waves produced upon the collapse of vapour structures, erosion-sensitive areas can be identified by analyzing the wall pressure peaks due to impacts of collapse induced shock-waves. Mihatsch et al. [42] studied the cavitating flow with an inviscid compressible density-based approach coupled with equilibrium cavitation model. They showed that the location of high pressure on the wall and the density of collapse events in their simulations agree well with the erosion damage pattern in the experiment of Franc et al. [40]. Mottyll and Skoda [43] studied the cavitating flow on the ultrasonic horn set-ups using a compressible inviscid flow solver with barotropic homogeneous cavitation model. The studied flow exhibits the characteristics of an attached cavity in hydrodynamic cavitation. Using the wall pressure load and collapse locations, Mottyll and Skoda [43] were able to predict the erosion pattern similar to the experiment and to identify the cavitation erosion mechanisms in the studied flow. Budich et al. [44] studied the cavitating flow over a propeller using an inviscid compressible density-based numerical approach combined with barotropic homogeneous cavitation model. Although the effect of viscosity was ignored, the results agreed well with the cavitation pattern in the experiment. They also investigated the aggressiveness of the cavitating flow [45] and showed that the collapse of cavitation structures close to trailing edge were associated with high risk of cavitation erosion in the studied flow.

1.5 Objectives and scope of this thesis

The objective of this thesis is to identify the hydrodynamic mechanisms of cavitation erosion in the cavitating flow over a NACA0009 foil using both experimental and numerical methods. To fulfill this objective, the following steps have been taken in this thesis.

- Detailed analysis of the shedding behavior using high-speed visualization and LES: Based on the literature review in section 1.2, it can be concluded that the knowledge of the shedding behavior of cavitating flows plays a crucial role in identifying the hydrodynamic mechanism of cavitation erosion. The cavitating flows studied here exhibits complex features, such as different types of re-entrant jets and detachment of small-scale cavitating structures from the sheet and cloud cavities. The comparison between the LES results and high-speed videos shows that the LES simulation is capable of capturing these complex features; therefore the LES results are then used to study details of the complex features of the cavitating flows over a NACA0009 foil.
- Erosion assessment using paint test: In this step, the locations of erosive collapse events are determined using a soft paint test method. The foil is painted with a thin layer of stencil ink and the location of paint removal is used to identify the location of erosive collapses. The procedure for the

paint test, including the painting procedure and the stencil ink used for the paint test, is briefly explained in chapter 2. The paint test results for two cavitation numbers are presented in the results section and the erosion patterns and locations of erosive collapse events in two cavitation numbers are compared.

- Investigation of the relationship between erosion pattern and cavitating structures: In this step, the detectable collapse events in high-speed videos and the erosion pattern obtained in the paint test are used to find the relationship between the erosion pattern and cavitating structures. The hydrodynamic process for the creation of these structures is determined using high-speed videos.
- Numerical assessment of cavitation erosion using a density-based compressible solver: To identify the risk of cavitation erosion numerically, a compressible solver which is capable of capturing the shock-wave upon the collapse of cavities, is implemented in the OpenFOAM framework. The solver is described and its validation is presented in chapter 2. The solver is then used to simulate the cavitating flow over the NACA0009 foil and the simulation results are compared with the high-speed visualization which shows that the solver is capable of capturing the main feature of the cavitating flow. The locations of collapse event with high collapse pressure are compared with the paint test which shows a qualitative agreement. Numerical simulation results are then used to identify the hydrodynamic mechanisms of erosive collapse events.

2

Methods

In this chapter, the experimental and numerical methods used in this thesis are described. The experimental methods include high-speed video observations and paint test, where in the former the dynamics of cavitating structures are recorded by a high speed camera and in the latter, the location of erosive collapse events are determined based on the removal of the ink layer which is applied on the surface of the foil. The numerical methods consist of two solvers, an incompressible pressure-based solver with transport-based mixture cavitation model and a compressible density-based solver with an equilibrium cavitation model. These solvers are described in this chapter. As the compressible density-based solver is implemented in the OpenFOAM framework within the scope of this thesis, the validation of this solver is also presented.

2.1 Modified NACA0009 foil case

The tested foil is a modified version of the NACA0009 foil with chord length, c , of 100 mm and span length of 150 mm. The profile of the foil can be described as,

$$\frac{y}{c} = \begin{cases} a_0 \left(\frac{x}{c}\right)^{\frac{1}{2}} + a_1 \left(\frac{x}{c}\right) + a_2 \left(\frac{x}{c}\right)^2 + a_3 \left(\frac{x}{c}\right)^3 & 0 \leq \frac{x}{c} \leq 0.45 \\ b_1 \left(1 - \frac{x}{c}\right) + b_2 \left(1 - \frac{x}{c}\right)^2 + b_3 \left(1 - \frac{x}{c}\right)^3 & 0.45 \leq \frac{x}{c} \leq 1 \end{cases} \quad (2.1)$$

where C is the foil chord and the coefficients, a and b , are given in table 2.1.

2.1.1 Experimental set-up

In the experimental part of the current study, the tested foil was installed in the EPFL high speed cavitation tunnel. A schematic image of this cavitation tunnel is shown in figure 2.1. This cavitation tunnel has a test section with dimensions of $0.15 \times 0.15 \times 0.75 m^3$ and it is capable of delivering velocity up to $50 m/s$ at the inlet of the test section. The operating condition of the experiment is controlled by

a_0	+0.173688	b_1	+0.1737
a_1	0.244183	b_2	0.185355
a_2	+0.313481	b_3	+0.33268
a_3	0.275571		

Table 2.1: Coefficients, a and b , in equation 2.1

upstream velocity, U , the incidence of angle of the foil, α , and cavitation number, σ . Here, we studied a cavitating flow with the upstream velocity of 20 m/s over the foil with 5° incidence angle. The cavitation number, σ , which is defined based on the pressure at inlet, is varied from 1.1 to 1.5. Figure 2.2 shows a schematic view of the experimental set-up and the operating conditions.

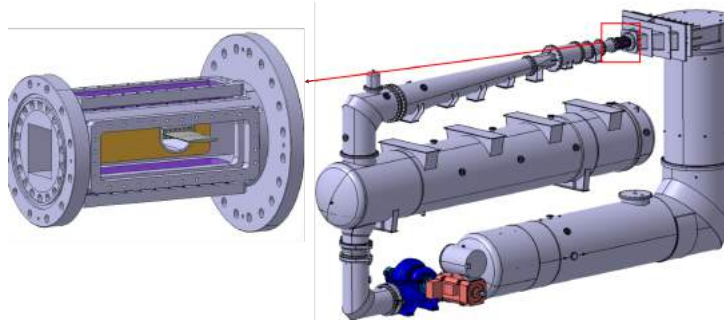


Figure 2.1: A schematic image of EPFL high speed cavitation tunnel

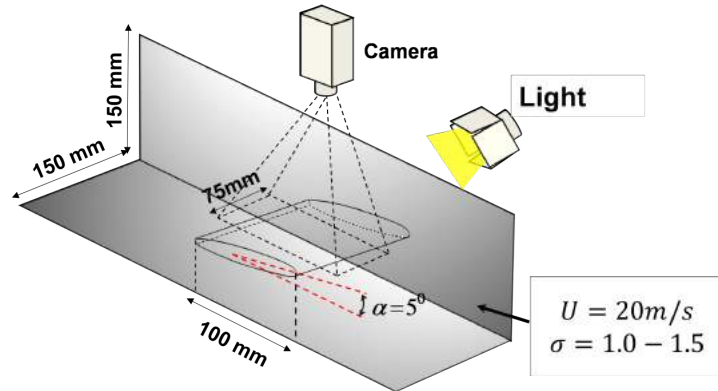
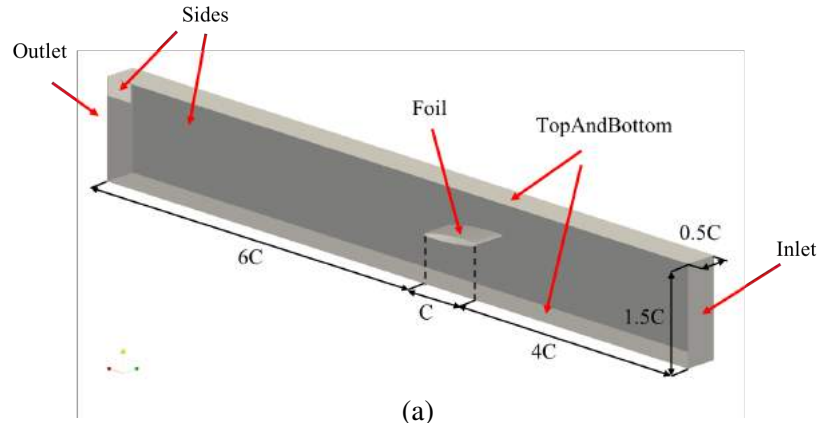


Figure 2.2: A schematic view of the experimental set-up and operating conditions



Boundary name	Incompressible Simulation				Compressible Simulation		
	P	U	α_l	v_{sgs}	P	U	α_l
Inlet	zeroGradient	fixedValue	fixedValue	zeroGradient	zeroGradient	fixedValue	fixedValue
Sides	zeroGradient	noSlip	zeroGradient	zeroGradient	zeroGradient	slip	zeroGradient
TopAndBottom	zeroGradient	noSlip	zeroGradient	wallFunction	zeroGradient	slip	zeroGradient
Foil	zeroGradient	noSlip	zeroGradient	wallFunction	zeroGradient	slip	zeroGradient
Outlet	fixedValue	zeroGradient	zeroGradient	zeroGradient	fixedValue	zeroGradient	zeroGradient

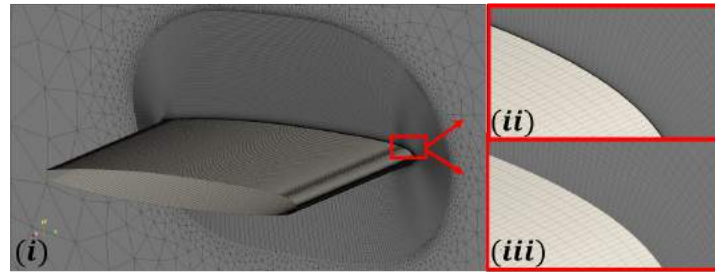


Figure 2.3: Computation configuration for the foil a) computation domain, b) definition of boundary conditions ,c-i) grid topology , c-ii) close view of grid spacing in the incompressible simulation, c-iii) close view of grid spacing in the compressible simulation

2.1.2 Computational domain and boundary conditions

In the next chapter, the simulation results of the cavitating flow with $\sigma = 1.25$ are presented. The computational domain and boundary conditions used in these simulations are shown in figure 2.3. The domain is a 3D channel with the height of $1.5c$ and width of $0.5c$. The height of computational domain is exactly the same as the height of the test section and its width is equal to one-third of the foil span to decrease the computational cost. The channel is extended $4c$ upstream of the foil leading edge and $6c$ behind of the trailing edge. Figure 2.3c-i shows the mesh topology used in the simulations. The domain is divided into two regions with different types of mesh. The region near the foil is discretized with a structured

hexahedral O-type mesh, and the outer region is discretized with an unstructured mesh. For incompressible simulation, the average y^+ around the foil is less than 1, and the maximum x^+ on the upper surface of the foil is around 300. The mesh resolution for the compressible simulation is similar to the incompressible simulation except for the region close to the foil surface where y^+ of 30 is used. The total number of the cells in the incompressible and compressible simulations are 9.72 and 7.35 millions, respectively.

2.2 High speed observation and paint test

The dynamics of cavitation is recorded by a high-speed camera (Photron FAST-CAM mini) from the top view, as shown in figure 2.2. The camera view is focused on the middle half of the foil to be able to record the videos with the frame rate of 10 kHz. To identify the areas with high risk of cavitation erosion, we use a simple paint test method, where the foil is covered with a layer of soft stencil ink. This method of erosion assessment have been used by many researchers, for instance Pfitsch et al. [46] and Cao et al. [10], and has become a standard method for the erosion assessment of newly-designed propellers. During the cavitation test, violent collapses of vapour structures near the surface removes the ink from the foil and the regions of paint removal serves as an indicator of areas with high erosion risk. Different methods of painting can be used to apply the ink on the surface of the foil. In this study, the ink layer is applied by dipping the foil along its span-wise axis into a container filled with Marsh Rolmark Roller Stencil Ink. The foil is let to dry in the same position at room temperature for a couple of hours. Figure 2.4a shows the status of the paint after it dried. As it can be seen, a uniform coating is obtained. In order to check the effect of dipping and the position of the foil when it is drying on the thickness of the ink layer, the thickness is measured using Elcometer 456 Coating Thickness Gauge over a line in span-wise direction, shown in figure 2.4a. Figure 2.4b shows the distribution of the ink thickness as a function of span-wise location. As expected, the ink layer is thicker near the tip of the foil, however an almost uniform thickness is obtained up to 70 percent of the span. Before each cavitation erosion test, the resistance of the ink layer against the shear of the flow is examined. The coated foil is tested at the flow velocity of 20m/s and non-cavitating condition and no paint removal due to the flow shear was observed.

2.3 Numerical methods

2.3.1 Pressure-based incompressible solver with TEM cavitation model

This solver is a modified version of interPhaseChangeFoam solver from OpenFOAM-2.2.x framework([47]) which has been used and validated for cavitating flows by Huuva [26], Bensow and Bark [25], Lu et al. [48], and Asnaghi and Bensow [49]. In this solver, each phase, liquid and vapour, is considered incompressible. The

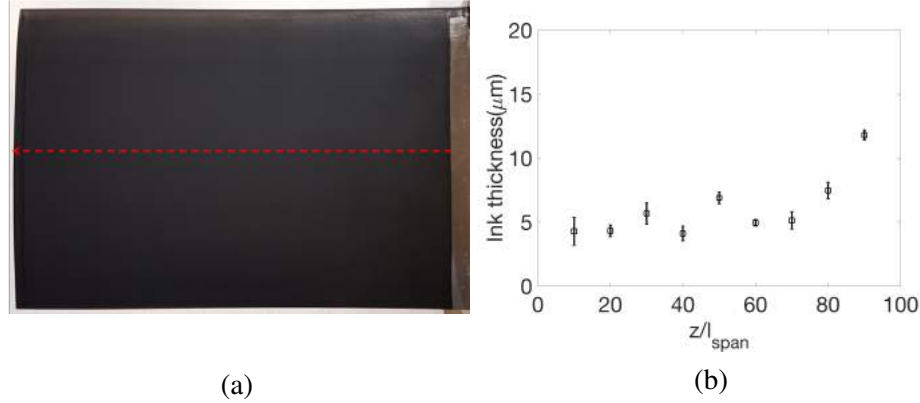


Figure 2.4: Foil coated with layer of stencil ink, a) status of ink layer before the cavitation test, b) thickness of the ink layer over dashed red line in (a)

two phase flow is assumed as a homogeneous mixture of two immiscible fluids. With this assumption, the mixture density, ρ_m , and viscosity, μ_m , can be expressed as,

$$\rho_m = \alpha_l \rho_l + (1 - \alpha_l) \rho_v, \quad \mu_m = \alpha_l \mu_l + (1 - \alpha_l) \mu_v, \quad (2.2)$$

where α_l is the liquid volume fraction, ρ_l and ρ_v are liquid and vapour density, and μ_l and μ_v are liquid and vapour viscosity. With the assumption that there is no slip between liquid and vapour, two phases share same velocity and pressure, therefore a single momentum equation can be used to obtain the velocity field. This equation reads as,

$$\frac{\partial(\rho_m u_i)}{\partial t} + \frac{\partial(\rho_m u_i u_j)}{\partial x_j} = -\frac{\partial p}{\partial x_i} + \frac{\partial \sigma_{ij}}{\partial x_j}, \quad (2.3)$$

in which p is static pressure and σ_{ij} is the viscous stress tensor that can be expressed as

$$\sigma_{ij} = \mu_m \left(\frac{\partial u_i}{\partial x_j} + \frac{\partial u_j}{\partial x_i} \right) - \frac{2}{3} \mu_m \frac{\partial u_k}{\partial x_k} \delta_{ij}. \quad (2.4)$$

Cavitation modeling

The cavitation dynamics is captured by Transport Equation Modelling (TEM), where a transport equation for liquid volume fraction, α_l , is solved,

$$\frac{\partial(\alpha_l)}{\partial t} + \frac{\partial(u_i \alpha_l)}{\partial x_j} = \frac{\dot{m}}{\rho_l}, \quad (2.5)$$

where \dot{m} is the mass transfer term which accounts for vaporization and condensation. Here, the Schnerr-Sauer cavitation model [50] is used to model this term. The source term is written as the summation of condensation, $\dot{m}_{\alpha_{lc}}$, and vaporization $\dot{m}_{\alpha_{lv}}$ terms as,

$$\dot{m} = \alpha_l (\dot{m}_{\alpha_{lv}} - \dot{m}_{\alpha_{lc}}) + \dot{m}_{\alpha_{lc}}, \quad (2.6)$$

where $\dot{m}_{\alpha_{lv}}$ and $\dot{m}_{\alpha_{lc}}$ are obtained from

$$\dot{m}_{\alpha_{lc}} = C_c \alpha_l \frac{3\rho_l \rho_v}{\rho_m R_B} \sqrt{\frac{2}{3\rho_l}} \sqrt{\frac{1}{|p - p_v|}} \max(p - p_v, 0), \quad (2.7)$$

$$\dot{m}_{\alpha_{lv}} = C_v (1 + \alpha_{Nuc} - \alpha_l) \frac{3\rho_l \rho_v}{\rho_m R_B} \sqrt{\frac{2}{3\rho_l}} \sqrt{\frac{1}{|p - p_v|}} \min(p - p_v, 0). \quad (2.8)$$

In equations 2.7 and 2.8, p_v is the vapour pressure, α_{Nuc} is the initial volume fraction of nuclei, and R_B is the radius of the nuclei which is obtained from

$$R_B = \sqrt[3]{\frac{3}{4\pi n_0} \frac{1 + \alpha_{Nuc} - \alpha_l}{\alpha_l}}. \quad (2.9)$$

The initial volume fraction of nuclei is calculated from

$$\alpha_{Nuc} = \frac{\frac{\pi n_0 d_{Nuc}^3}{6}}{1 + \frac{\pi n_0 d_{Nuc}^3}{6}}, \quad (2.10)$$

where the average nuclei per liquid, n_0 , and the initial nuclei diameter, d_{Nuc} , are assumed to be 10^{12} and $10^{-4}m$, respectively.

Turbulence modeling

The effect of turbulence is considered using an Implicit Large Eddy Simulation (ILES) approach where a low pass filter is applied to the governing equations. The filtered momentum equation is then written as,

$$\frac{\partial(\rho_m \bar{u}_i)}{\partial t} + \frac{\partial(\rho_m \bar{u}_i \bar{u}_j)}{\partial x_j} = -\frac{\partial \bar{p}}{\partial x_i} + \frac{\partial \bar{\sigma}_{ij}}{\partial x_j} - \frac{\partial B_{ij}}{\partial x_j}, \quad (2.11)$$

where overbar denotes filtered variables and $B_{ij} = \rho_m(\bar{u_i u_j} - \bar{u_i} \bar{u_j})$ is the subgrid stress tensor. In ILES approach, no explicit model is provided for B_{ij} and it is assumed that the numerical dissipation mimics the effect of this term. This approach has been successfully applied in the simulation of non-cavitating and cavitating flows (Huuva [26], Bensow and Bark [25], Lu et al. [48], and Asnaghi and Bensow [49]).

2.3.1.1 Discretization scheme and solution algorithm

The convective terms and diffusion term in the momentum equations are discretized respectively using a TVD limited linear interpolation scheme with the limiter value of 0.5 and standard linear interpolation. The convective term in the liquid fraction is discretized using a first order upwind scheme. For time discretization, a second order implicit scheme is used. The discretized equations are solved using a pressure-based PIMPLE approach. More details about the solution procedure can be found in Asnaghi and Bensow [49] and Bensow and Bark [25].

2.3.2 Density-based compressible solver with equilibrium cavitation model

In this solver, the two-phase flow is assumed to be a homogeneous mixture of liquid and vapour. The flow is governed by the compressible Euler equations, i.e.,

$$\frac{\partial \mathbf{U}}{\partial t} + \nabla \cdot \mathbf{F}(\mathbf{U}) = 0, \quad (2.12)$$

where $\mathbf{U} = \{\rho, \rho u_1, \rho u_2, \rho u_3, \rho E\}^T$ represents the vector of conserved variables and $\mathbf{F}(\mathbf{U})$ represents the tensor of inviscid fluxes. Here, ρ is density, $\{u_1, u_2, u_3\}$ is the velocity vector, and E is the total specific energy which is the summation of specific internal energy, e , and specific kinetic energy, $\frac{1}{2}u \cdot u$. The inviscid flux tensor, $\mathbf{F} = \{F_1, F_2, F_3\}$, is described as,

$$F_1 = \begin{bmatrix} \rho u_1 \\ \rho u_1^2 + p \\ \rho u_1 u_2 \\ \rho u_1 u_3 \\ \rho u_1 (E + p/\rho) \end{bmatrix}, \quad F_2 = \begin{bmatrix} \rho u_2 \\ \rho u_2 u_1 \\ \rho u_2^2 + p \\ \rho u_2 u_3 \\ \rho u_2 (E + p/\rho) \end{bmatrix}, \quad F_3 = \begin{bmatrix} \rho u_3 \\ \rho u_3 u_1 \\ \rho u_2 u_3 \\ \rho u_3^2 + p \\ \rho u_3 (E + p/\rho) \end{bmatrix}. \quad (2.13)$$

Equations 2.12 are solved using a density based approach which gives the vector of conserved variable, \mathbf{U} . In order to close the governing equations and obtain other variables such as pressure, temperature, and liquid or vapour fraction, an equilibrium cavitation model coupled with a suitable equation of state (EOS) is used.

Equilibrium cavitation model

In the equilibrium cavitation model, the two-phase mixture density is assumed as weighted summation of vapour saturation density, $\rho_{v,sat}$, and liquid saturation density, $\rho_{l,sat}$,

$$\rho = \alpha_v \rho_{v,sat} + (1 - \alpha_v) \rho_{l,sat}, \quad (2.14)$$

where α_v is the vapour volume fraction. By substituting the density obtained from solving governing equations 2.12 and the saturation densities into equation 2.14, the vapour volume fraction can be obtained. In order to obtain pressure and temperature, two equation of states are implemented. These equations are presented in the following sections.

Temperature-Dependent EOS

If the effect of temperature variation is taken into account, the equation of states should give the equations for pressure and temperature as a function of internal energy and density.

$$p = p(\rho, e), \quad T = T(\rho, e) \quad (2.15)$$

In cavitating flows, three states can exist in the flow simultaneously, therefore three equations of state should be provided. These states are pure liquid, pure vapour and liquid-vapour mixture. If the density obtained by solving the governing equation is above liquid saturated density ($\rho > \rho_{l,sat}$), the flow is assumed to be in the liquid state and the vapour volume fraction is assumed to be 0. The pressure is then obtained from modified Tait equation of state [51],

$$p = B \left[\left(\frac{\rho}{\rho_{sat}(T)} \right)^N - 1 \right] + p_{sat}(T), \quad (2.16)$$

and the temperature is calculated from

$$T = \frac{e - e_{l0}}{c_{v,l}} + T_{ref}. \quad (2.17)$$

When the density drops below the vapour saturated density ($\rho < \rho_{v,sat}$), the flow is assumed to be in the vapour state and vapour fraction is assumed to be 1. The perfect gas equation of state is then used to obtain the pressure,

$$p = \rho RT \quad (2.18)$$

and the temperature is obtained from

$$T = \frac{e - e_{l0} - L_{v,ref}}{c_{v,v}} + T_{ref}. \quad (2.19)$$

In case that the density is between the vapour saturated density and liquid saturated density, the flow is assumed to be in a mixture state. Following the equilibrium condition in this state, the pressure is equal to the vapour pressure,

$$p = p_{sat}(T), \quad (2.20)$$

and the volume fraction, α , is obtained from

$$\alpha = \frac{\rho - \rho_{l,sat}}{\rho_{v,sat} - \rho_{l,sat}}. \quad (2.21)$$

The temperature in the mixture is calculated as,

$$T = \frac{\rho(e - e_{l0}) - \alpha \rho_{v,sat} L_{v,ref}}{\rho_{v,sat} \alpha c_{v,v} + \rho_{l,sat} (1 - \alpha) c_{v,l}} + T_{ref}. \quad (2.22)$$

The parameters in equations 2.16, 2.17, 2.20, 2.21, and 2.22 are given table 2.2. IAPWS-IF97 library [52] are used to obtain the saturated pressure, p_v and saturated liquid and vapour density, $\rho_{l,sat}$ and $\rho_{v,sat}$, in the above equations.

Table 2.2: Parameters in equations 2.16- 2.22

N	7.15	e_{l0}	$617e_{l0}(Kg^{-1})$
K_0	$3.06 \times 10^8 \text{ pa}$	R	$461.1 JKg^{-1}K^{-1}$
$c_{v,l}$	$4180 JKg^{-1}K^{-1}$	$c_{v,v}$	$1410.8 JKg^{-1}K^{-1}$
T_{ref}	273 K	$l_v(T_{ref})$	$2.753 \times 10^6 JKg^{-1}K^{-1}$

Table 2.3: Parameters in equation 2.24, 2.21, and Tait equation of state (equation 2.16) for barotropic EOS

p_{sat}	2340 <i>pa</i>	B	$3.06 \times 10^8 \text{ pa}$
$\rho_{l,sat}$	998.2 kg/m^3	$\rho_{v,sat}$	0.01389 kg/m^3
N	7.1	C	1480 $Pa kg/m^3$

Barotropic EOS

With the barotropic assumption, the pressure is assumed to depend only on density,

$$p = p(\rho). \quad (2.23)$$

Therefore the temperature becomes decoupled from other variables and there is no need to solve the energy equation. For the pure liquid phase, the pressure is obtained from the Tait equation of state (equation 2.16) with the assumption that saturated densities are constant. For the mixture phase, the barotropic equation proposed by Egerer et al. [53] is used. This equation is derived by assuming that the vaporization/condensation process is isentropic and reads as,

$$p = p_{sat} + C \left(\frac{1}{\rho_{l,sat}} - \frac{1}{\rho} \right). \quad (2.24)$$

The parameters in equations 2.24 and 2.21 are defined in Table 2.3.

2.3.2.1 Numerical method

The governing equations 2.12 are solved using a cell centered co-located finite volume (FV) method with arbitrary cell-shapes. These equations are integrated over the volume of the cell, Ω_i ,

$$\frac{\partial \bar{U}_i}{\partial t} + \frac{1}{|\Omega_i|} \sum_{j=1}^{N_i} \hat{F}(\bar{U}_L, \bar{U}_R, \mathbf{n}) |S_{ij}| = 0, \quad (2.25)$$

where $|\Omega_i|$ is the volume of the cell, N_i is number of faces belonging to the cell, $|S_{ij}|$ is the area of face j , \bar{U}_i is the volume-averaged conserved variable vector over the cell,

$$\bar{U}_i = \frac{1}{|\Omega_i|} \int_{\Omega_i} \mathbf{U} dV, \quad (2.26)$$

and $\bar{\mathbf{U}}_L$ and $\bar{\mathbf{U}}_R$ are the left and right states of face j , and \mathbf{n} is the normal vector of the face j . The inviscid flux normal to the faces, $\hat{F}(\bar{\mathbf{U}}_L, \bar{\mathbf{U}}_R, \mathbf{n})$, are calculated using the Mach consistent numerical flux scheme by Schmidt [54]. In this scheme, the inviscid flux normal to the face j is obtained as,

$$\hat{F}(\bar{\mathbf{U}}_L, \bar{\mathbf{U}}_R, \mathbf{n}) = (\rho_m)_{L/R} u_{fj} \begin{pmatrix} 1 \\ (u_1)_{L/R} \\ (u_2)_{L/R} \\ (u_3)_{L/R} \end{pmatrix} + \begin{pmatrix} 0 \\ p_{fj} n_{j,x} \\ p_{fj} n_{j,y} \\ p_{fj} n_{j,z} \end{pmatrix}, \quad (2.27)$$

where u_{fj} and p_{fj} are, respectively, the flux speed and pressure at the face j and $(\rho_m)_{L/R}$, $(u_1)_{L/R}$, $(u_2)_{L/R}$, and $(u_3)_{L/R}$ are density and velocities in the left or right state depending on the sign u_{fj} (for $u_{fj} > 0$, $()_{L/R} = ()_L$, otherwise $()_{L/R} = ()_R$). The flux speed, u_{fj} , and pressure, p_{fj} , are calculated from

$$u_{fj} = \left(\frac{1}{\rho_L + \rho_R} \right) \left(\rho_L q_L + \rho_R q_R + \frac{p_L - p_R}{c_{fj}} \right), \quad p_{fj} = \frac{p_L + p_R}{2}, \quad (2.28)$$

where $q_{L/R}$ is the velocity normal to face j and c_{fj} is the speed of sound at the face j which is obtained as,

$$c_{fj} = \max(c_L, c_R). \quad (2.29)$$

The speed of sound in pure liquid and pure vapour, c_l and c_v , are assumed to be constant and equal to the speed of sound in the saturated liquid and vapour at the temperature of 293K. The speed of sound in the mixture, c_m , is obtained from Wallis formula [55] as,

$$\frac{1}{\rho_m c_m^2} = \frac{1 - \alpha_l}{\rho_{v,sat} c_v^2} + \frac{\alpha_l}{\rho_{l,sat} c_l^2}. \quad (2.30)$$

The left and right states of the faces, $()_L$ and $()_R$, are obtained using a second order reconstruction method with limiter of Venkatakrishnan [56]. For time advancing, an explicit low storage 2nd order Runge-Kutta schemes is employed. The described numerical methods are implemented in the OpenFOAM framework.

2.3.2.2 Numerical erosion assessment

As the implemented solver is capable of capturing shock waves produced upon the collapse of vapour structures, erosion-sensitive areas can be identified by analyzing the wall pressure peaks due to impacts of collapse induced shock-waves. Here, the maximum recorded pressure on each surface element of the foil is used to identify the areas with high risk of cavitation erosion. In order to obtain the frequency and the location of the erosive collapse events, the collapse detector developed by Mihatsch et al. [42] is applied. This method detects collapse events and estimates their collapse strength based on the maximum pressure upon the collapse. The algorithm of this method can be summarized as follows,

ρ_L, p_L, u_L			ρ_R, p_R, u_R		
p_L (<i>pa</i>)	u_L (<i>m/s</i>)	ρ_L (<i>kg/m³</i>)	p_R (<i>pa</i>)	u_R (<i>m/s</i>)	ρ_R (<i>kg/m³</i>)
1.0×10^8	-100	1038.76	$1e \times 10^8$	100.0	1038.76

Figure 2.5: Initial conditions and computational domain for 1D Cavitating flow

- At each time step, a list of cells, called candidate cell list, is created with the conditions that liquid fraction of the cell at the current time step should be one, $\alpha_l = 1$ and the liquid fraction at the previous time step should be less than 1, $\alpha_{l,old} < 1$. The cells in this list are considered the candidate cells in which the collapse of a cavity has occurred.
- The cells in the candidate cells list that have neighboring cells filled with liquid are considered to contain the last stage of an isolated collapse event.
- The pressure at the cells containing the collapse events are recorded when the divergence of velocity changes its sign from negative to positive.
- Collapse strength is estimated by the maximum pressure at the collapse centre

2.3.2.3 Validation

In order to validate the implemented solver, two simple cavitating flows are simulated. The first case is a 1D-cavitating flow which has been used by several authors (Gnanaskandan and Mahesh [57], Zheng et al. [58]) for validation of the solver for cavitating flows. The purpose of simulating this test case is to check the capability of the implemented methods in tracking a pressure discontinuity in compressible water flows. The computational domain is a tube with the length of 1 meter. The domain is discretized with 400 cells. At the beginning of the simulation, the tube is filled with liquid water and a diaphragm at the centre of the tube separates two flows in opposite directions with the same velocity magnitude. The initial conditions are shown in figure 2.5. When the diaphragm is removed, two expansion waves originate from the diaphragm location and travel toward left and right. Behind these expansion waves, the pressure drops and if the pressure drops to a small value, the flow starts to cavitate.

Figure 2.6 shows the solution at $t = 0.0002s$ in the numerical simulation and analytical solution obtained by Liu et al. [12]. It can be seen that no oscillation in the numerical simulation results around region with high gradient of velocity and pressure is observed. The comparison between analytical solution and numerical simulations results demonstrates that the implemented methods are capable of simulating 1D cavitating flow.

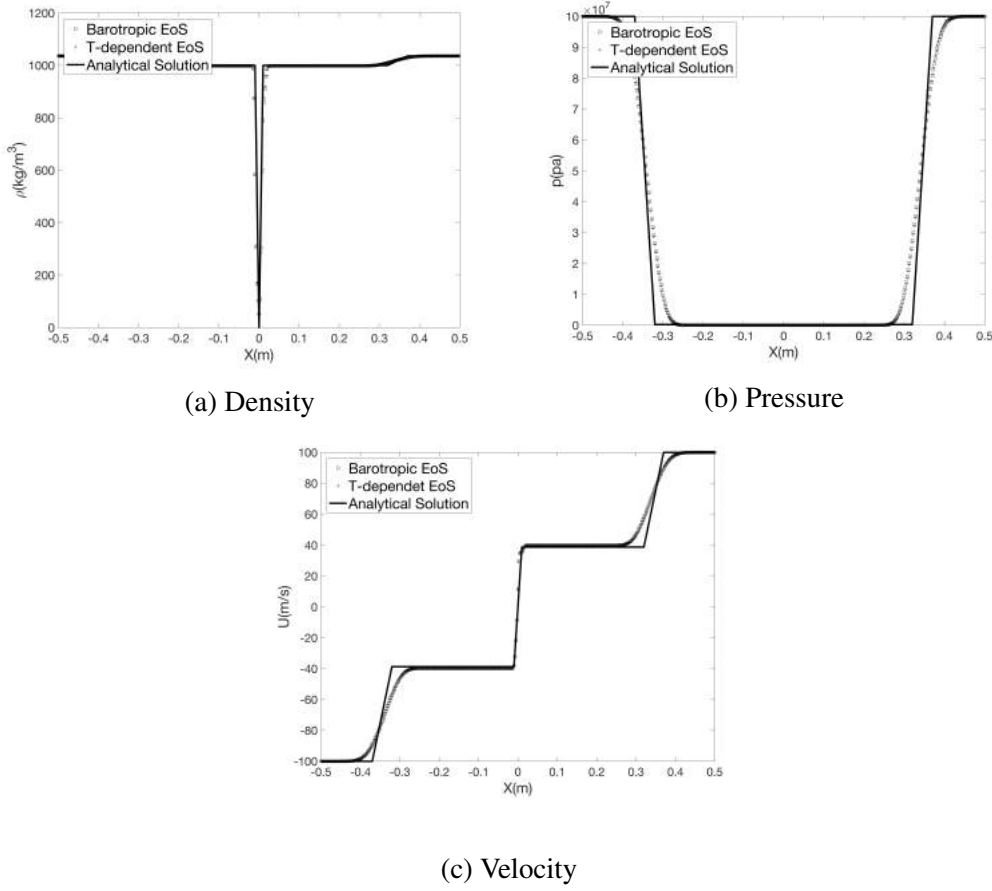


Figure 2.6: Comparison between the numerical solution and analytical solution[12] for a 1D cavitating flow

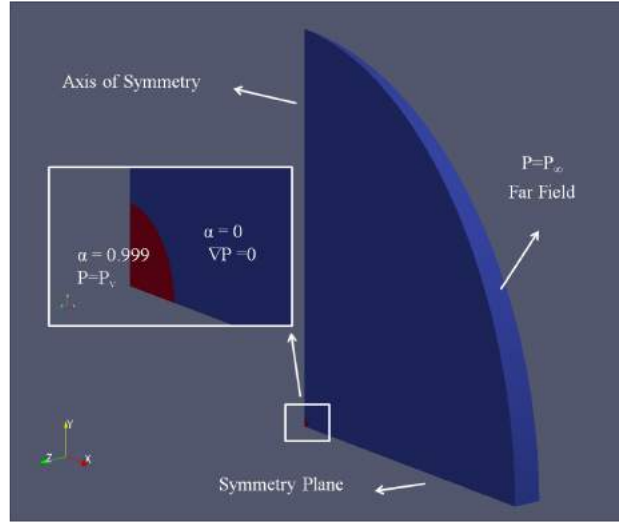
The second test case is the collapse of a spherical bubble in ambient pressure. The computational domain and boundary conditions are shown in figure 2.7a. To minimize the computational cost, an asymmetric wedge mesh with the angle of five degrees is created. The mesh is a section of a sphere and has 100 cells in the radial direction and 100 cells in the circumferential direction. The mesh spacing is very refined near the location of bubble collapse in order to capture the rapid movement of the bubble interface. As the initial conditions, the pressure inside the bubble is set to $p_v = 2340Pa$, while the pressure in the surrounding is set by solving the equation

$$\nabla p = 0 ; p(r = R_b) = p_v , p(r = 50R_b) = p_\infty. \quad (2.31)$$

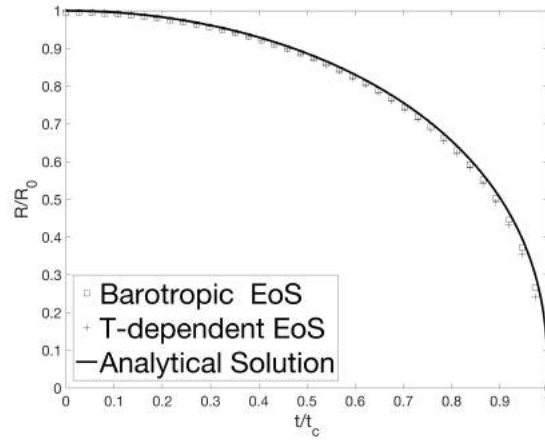
The analytical equation for the evolution of a spherical bubble in an infinite incompressible liquid is the Rayleigh-Plesset equation [59]. If we assume that the effect of viscosity, surface tension, and the gas inside the bubble are negligible, this equation reads

$$R\ddot{R} + \frac{3}{2}\dot{R}^2 = \frac{p_v - p_\infty}{\rho_l}, \quad (2.32)$$

where R is the bubble radius, p_v is the vapour pressure, p_∞ is the pressure in the far-field, and ρ_l is the density of the surrounding liquid. To compare numerical results with the solution of the Rayleigh equation, this equation is solved using the ODE solver in OpenFOAM. Figure 2.7b shows the time history of bubble radius in both simulation results and the Rayleigh solution. A good agreement between the results of both solvers and analytical solution is obtained which indicates that the implemented methods are valid.



(a)



(b)

Figure 2.7: Simulation of a collapsing bubble a) computational domain and BCs for the collapsing bubble case, b) comparison of numerical simulation and solution of equation 2.32 for a collapsing bubble.

3

Results

In this section, the results from high speed visualization (HSV), paint test, and numerical simulations are presented. The HSV shows that the evolution of cavitating structures are governed by two types of shedding, the shedding of the large scale cloud structures due to re-entrant jet and the shedding of small vapour structures from the closure line of sheet cavity and the downstream end of the cloud cavity. Following the study by Foeth et al. [21], we call the first type of shedding primary shedding and the second type of shedding secondary shedding.

3.1 Primary shedding

The analysis based on the HSV reveals that the primary shedding is governed by the Strouhal number

$$St = \frac{fl_{max}}{U_{\infty}} \quad (3.1)$$

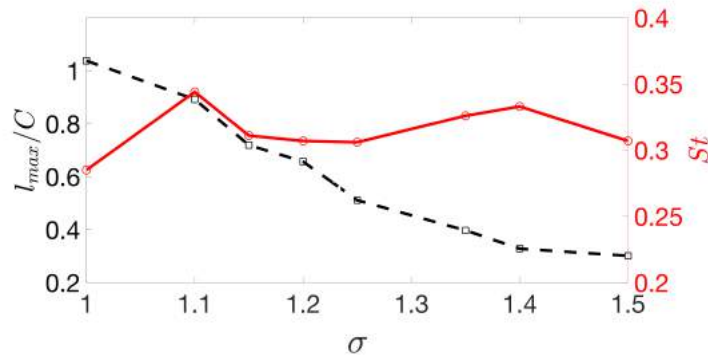


Figure 3.1: The variation of maximum length of sheet cavity and Strouhal number as function of cavitation number

where f is the shedding frequency, l_{max} is the maximum length of the sheet cavity, and U_∞ is the free stream velocity. Figure 3.1 shows the variation of maximum length of the sheet cavity and the Strouhal number as a function of cavitation number. It can be seen that the Strouhal number falls in the range of 0.2-0.4. This range is in agreement with the reported range for shedding of cloud cavitation due to re-entrant jet in the literature. In figure 3.1, it can also be seen that the maximum length of the cavity decreases as the cavitation number increases. It is interesting to note that the sensitivity of the maximum length of the cavity to the change in cavitation number is not uniform for different cavitation numbers and this sensitivity decreases as cavitation number increases.

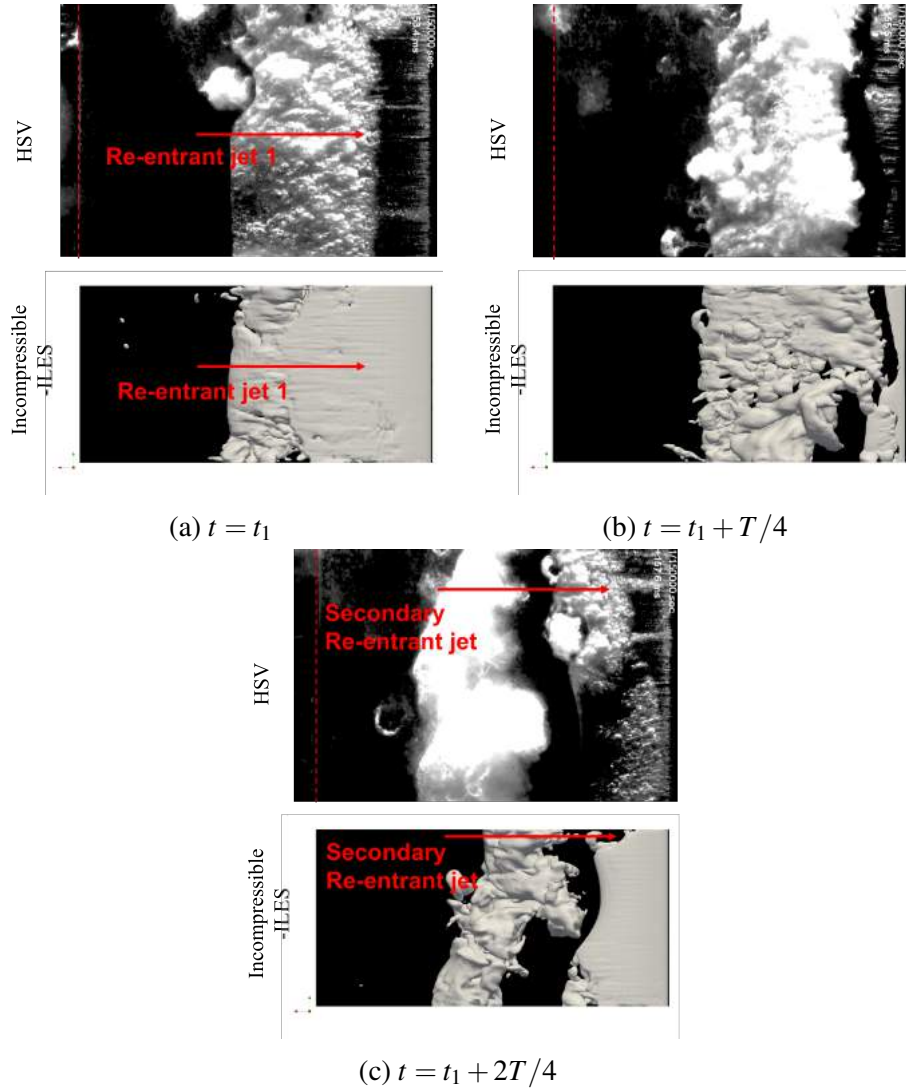


Figure 3.2: Primary shedding in HSV and numerical simulation for the cavitating flow with $\sigma = 1.25$ (Flow is from right to left and the trailing edge is marked by dashed red line).

Figure 3.2 shows the primary shedding in the cavitating flow with $\sigma = 1.25$ for two subsequent cycles. At time t_1 , the sheet cavity has reached its maximum length and a re-entrant jet has been created at the closure line of the sheet. The front of this re-entrant jet (marked by red arrow) can be detected on the interface of the sheet cavity. This re-entrant jet moves upstream and hits the interface of the sheet cavity at the leading edge as it is shown at time $t_1 + T/4$. It can also be seen that the collision of the re-entrant jet causes the pinch-off of a cloud cavity and that a new sheet cavity is formed on the leading edge of the foil. At time $t_1 + 2T/4$, the sheet cavity is growing and another re-entrant jet is formed at the closure line of the sheet cavity. We refer this re-entrant jet as the secondary re-entrant jet. The possible mechanism for the creation of this re-entrant jet will

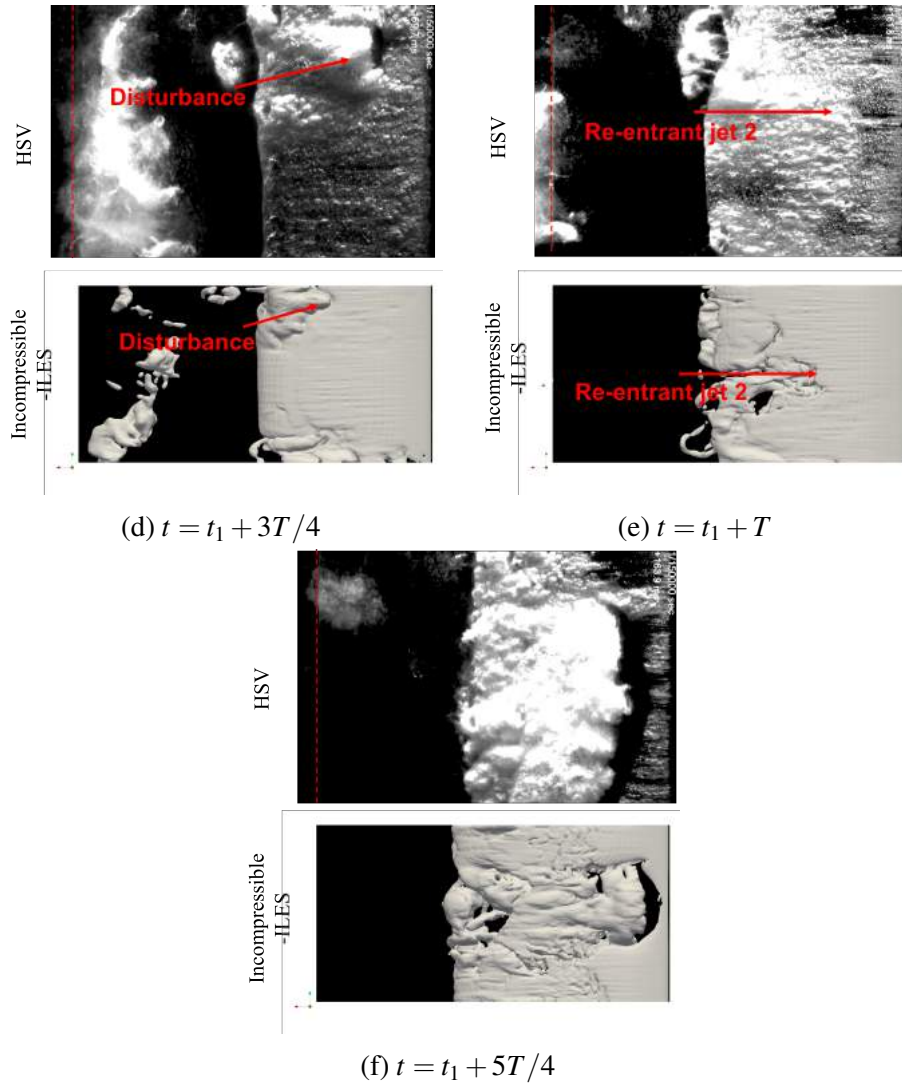


Figure 3.2: Primary shedding in HSV and numerical simulation for the cavitating flow with $\sigma = 1.25$ (Flow is from right to left and the trailing edge is marked by dashed red line).

be explained in section 3.1.1. Between instants $t_1 + 2T/4$ and $t_1 + 3T/4$, the secondary re-entrant jet has collided with the interface of the sheet cavity and created a disturbance on this interface. The sheet cavity then reaches its maximum length again at time $t_1 + T$ and re-entrant jet 2 is formed at the closure line. It can also be seen that the disturbance created by the secondary re-entrant jet has grown larger and reached the closure line of the sheet cavity. This disturbance can lead to the detachment of a cavity structure from the closure line and it is one mechanism for the secondary shedding which will be explained in more detail in section 3.2. The comparison between re-entrant jet 1 and re-entrant 2 shows that the front line of the re-entrant jet 1 is almost two-dimensional while the front line of the re-entrant jet 2 is entirely three-dimensional. The reason for this difference

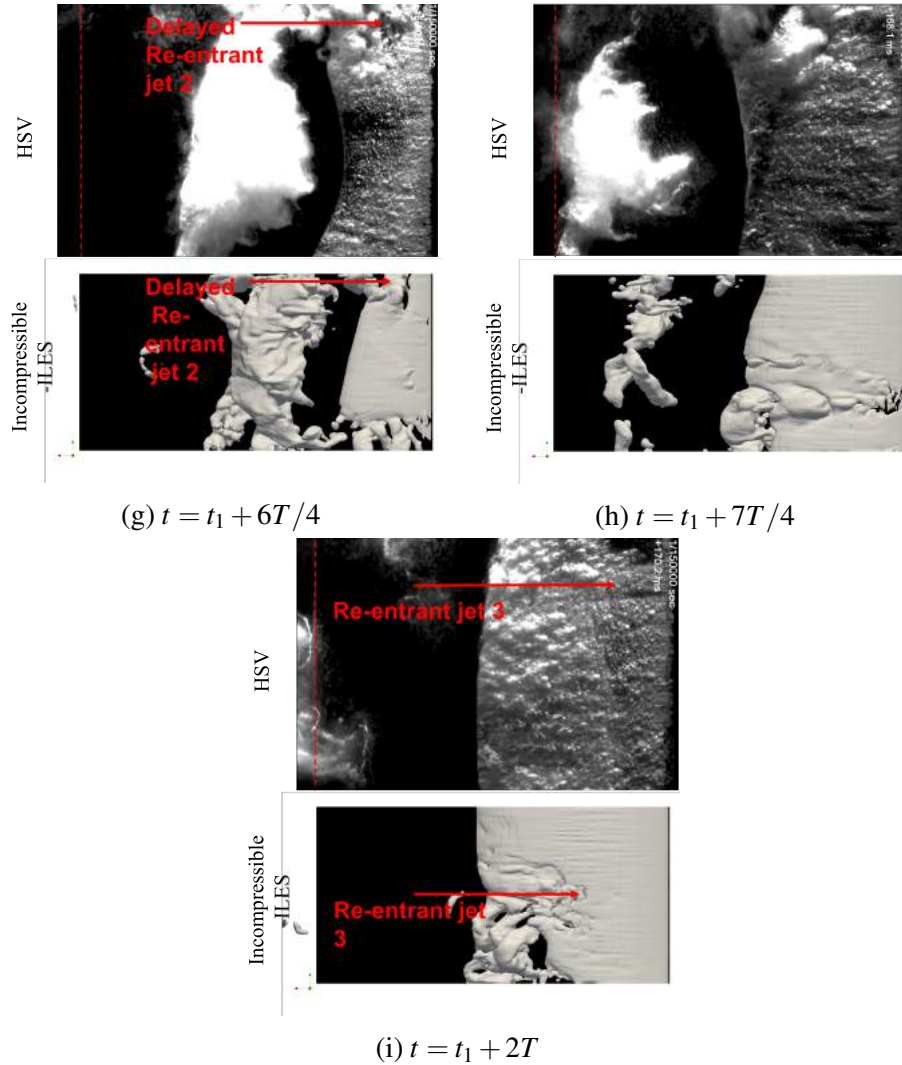


Figure 3.2: Primary shedding in HSV and numerical simulation for the cavitating flow with $\sigma = 1.25$ (Flow is from right to left and the trailing edge is marked by dashed red line).



Figure 3.3: Complex shedding behavior due to the delay in the formation of re-entrant jet (Flow is from right to left).

is that the formation of the re-entrant jet 2 at some span-wise location is delayed. The cause of this delay is explained in section 3.5. Due to this delay, it can be seen in figure 3.2 that a portion of re-entrant jet 2 reaches the leading edge at time $t_1 + 5T/4$ while the delayed part of the re-entrant jet 2 hits the interface at time $t_1 + 6T/4$. The collision between the delayed part of the re-entrant jet 2 and the interface of the sheet cavity creates a disturbance on the sheet cavity interface at time $t_1 + 6T/4$, similar to the disturbance created by the secondary re-entrant jet. This disturbance detaches from the closure of the sheet cavity as the sheet cavity grows to the maximum length. This detachment can be seen in the numerical simulation results and HSV, respectively, at instants $t_1 + 7T/4$ and $t_1 + 2T$. In the numerical simulation results, this detachment leads to the delay in the formation of re-entrant jet 3 at the location of the detachment, which can be seen at time $t_1 + 2T$. In the HSV, the sheet cavity at the location of disturbance is longer compared to other span-wise location. Therefore it is expected that the re-entrant jet 3 at the location of disturbance starts earlier. However, due to the effect of the disturbance on the pressure field around the closure line, the formation of the re-entrant 3 at the location of disturbance is delayed, therefore the front of the re-entrant jet 3 becomes almost two-dimensional at time $t_1 + 2T$. It should be mentioned that according to HSV, the delay in the formation of the re-entrant jets can lead to a complex shedding behavior where a highly three-dimensional re-entrant jet hits the interface of the sheet cavity. Figure 3.3 shows an example of this complex shedding behavior in HSV.

The comparison between the results of incompressible solver and the experimental high-speed visualization in figure 3.2 shows that the numerical simulation with the current set-up and grid resolution is able to capture the main features of the cavitating flow.

3.1.1 Secondary re-entrant jet

Figure 3.4 shows the instants corresponding to the formation of the secondary re-entrant jet in the numerical simulation results and HSV. At time $t_1 + 5T/4$, the cloud cavity has been detached from the leading edge and it is rolling down-

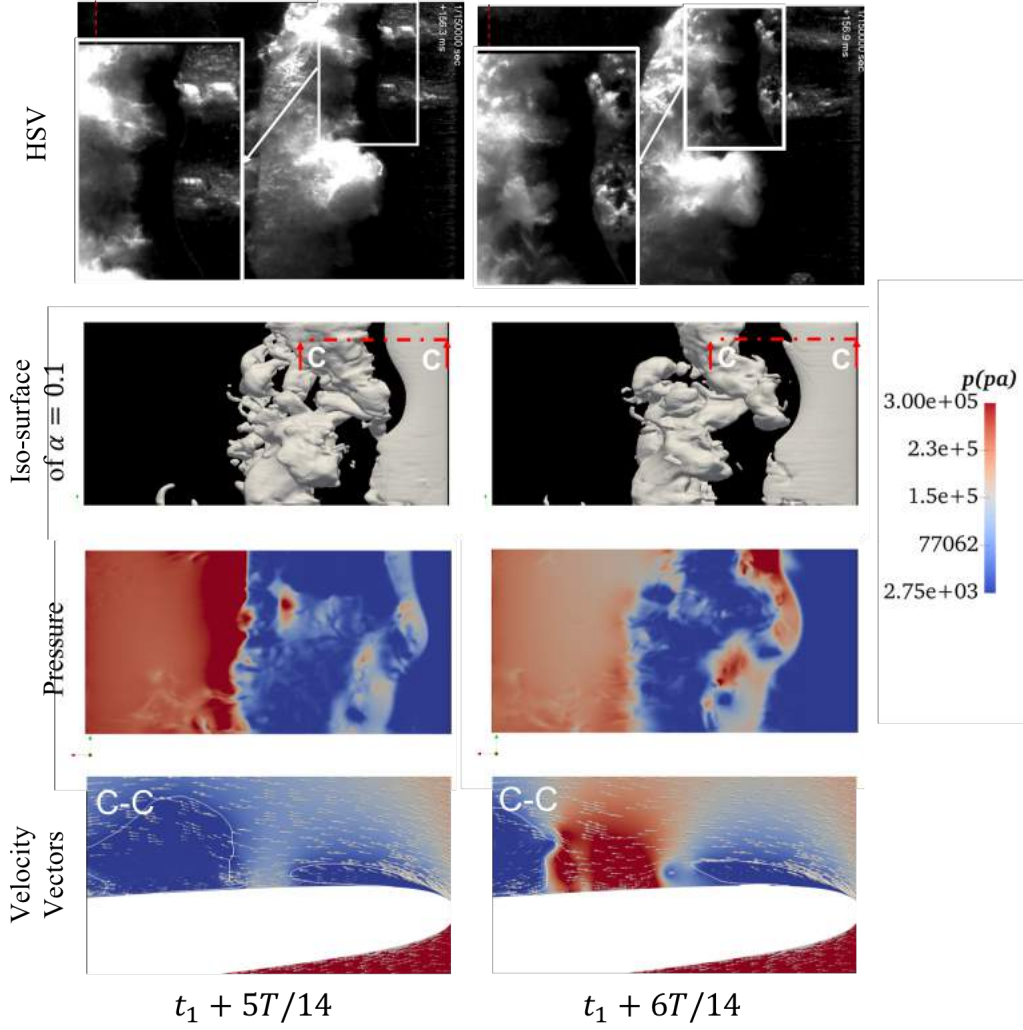


Figure 3.4: Instants corresponding to the formation of secondary re-entrant jet

stream. At the same time, a new sheet cavity appears at the leading edge. Between instants $t_1 + 5T/14$ and $t_1 + 6T/14$, the collapse of some vapour structures in the upstream part of the cloud can be seen in the zoom-in views of the HSV. At the same time, a pressure increase can be seen in the region between the closure line of the sheet cavity and the upstream part of the cloud in the numerical simulation results. One possible explanation for this high pressure can be a high condensation rate in the upstream part of the cloud. The high pressure at the closure line increases the adverse pressure gradient locally which in turn leads to the formation of secondary re-entrant jet. This re-entrant jet can be observed in the velocity vectors at time $t_1 + 2T/4$. The influence of the collapse of cloud structures on the dynamics of the sheet cavity has been also observed in the experimental study by Leroux et al. [60]. They showed that the pressure wave due to the collapse of

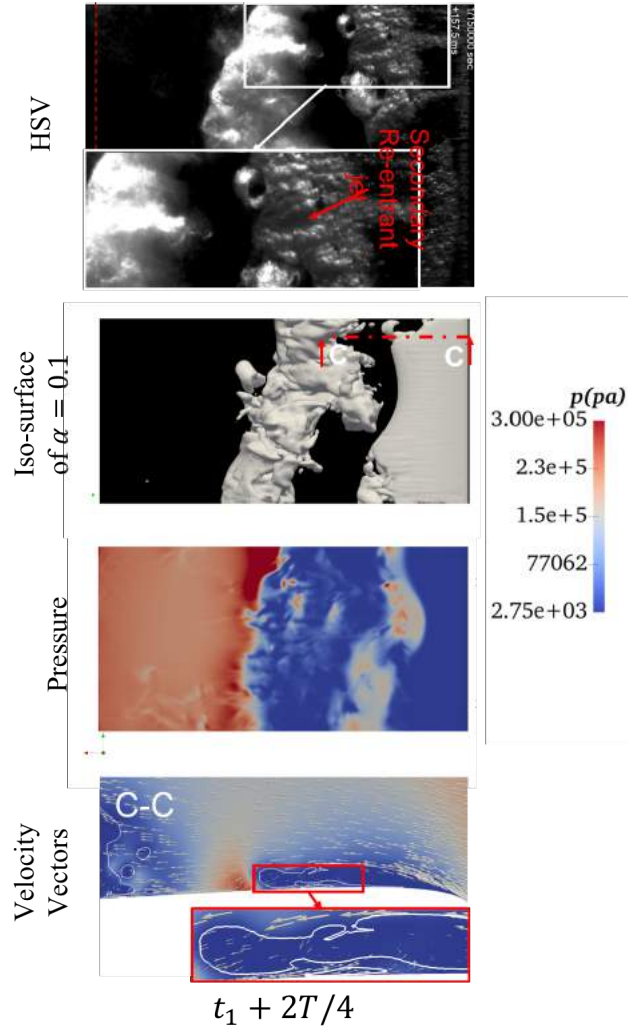


Figure 3.4: Instants corresponding to the formation of secondary re-entrant jet.

the large-scale cloud close to the trailing edge can lead to the disappearance of the newly formed sheet cavity. In the current study, the pressure increase is due to collapse of small cloud structures in the upstream of the cloud; therefore this pressure increase is not strong enough to remove the sheet cavity from the leading edge and it only leads to the formation of a secondary re-entrant jet.

3.1.2 Delay in the formation of main re-entrant jet

As mentioned in section 3.1, the detachment of structures from the closure line of the sheet cavity when it reaches its maximum length, can delay the formation of the re-entrant jet at the location of disturbance. An example of this delay is presented in figure 3.5 where the instants related to the formation of the re-entrant jet 2 in figure 3.2 are shown. At time $t_1 + 17T/21$, when the disturbance created by

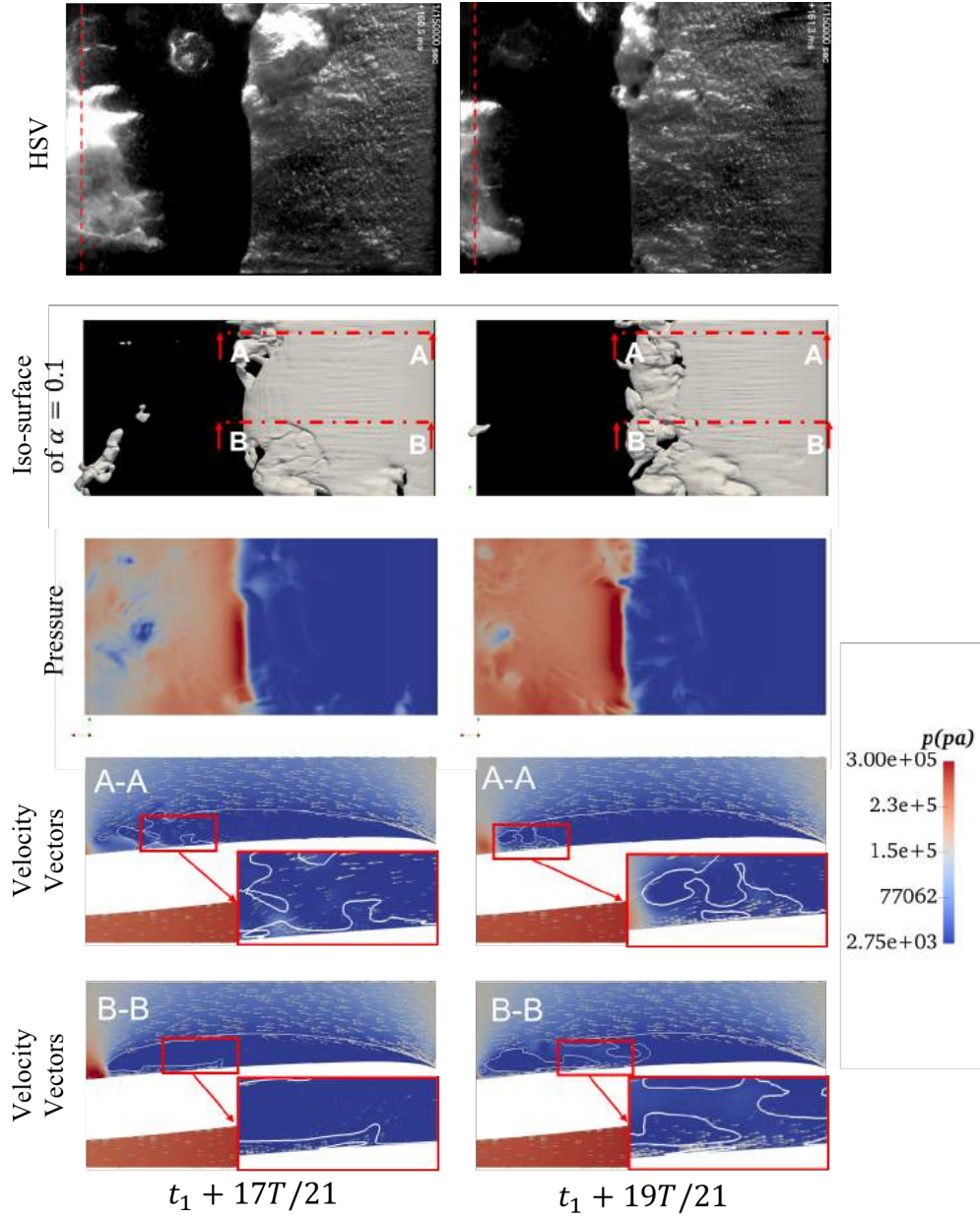


Figure 3.5: Delay in the formation of re-entrant jet 2

the secondary re-entrant jet reaches the closure line of the sheet cavity, it affects the flow field around the closure line of sheet cavity which can be seen in the flow field on the A-A plane at time $t_1 + 17T/21$. This disturbance leads to a lower pressure and consequently a lower adverse pressure gradient at its location compared to the other region of the closure line which in turn delays the formation of the re-entrant jet 2 in the region of disturbance. This delay can be seen in velocity vectors on the plane A-A and B-B at time $t_1 + T$.

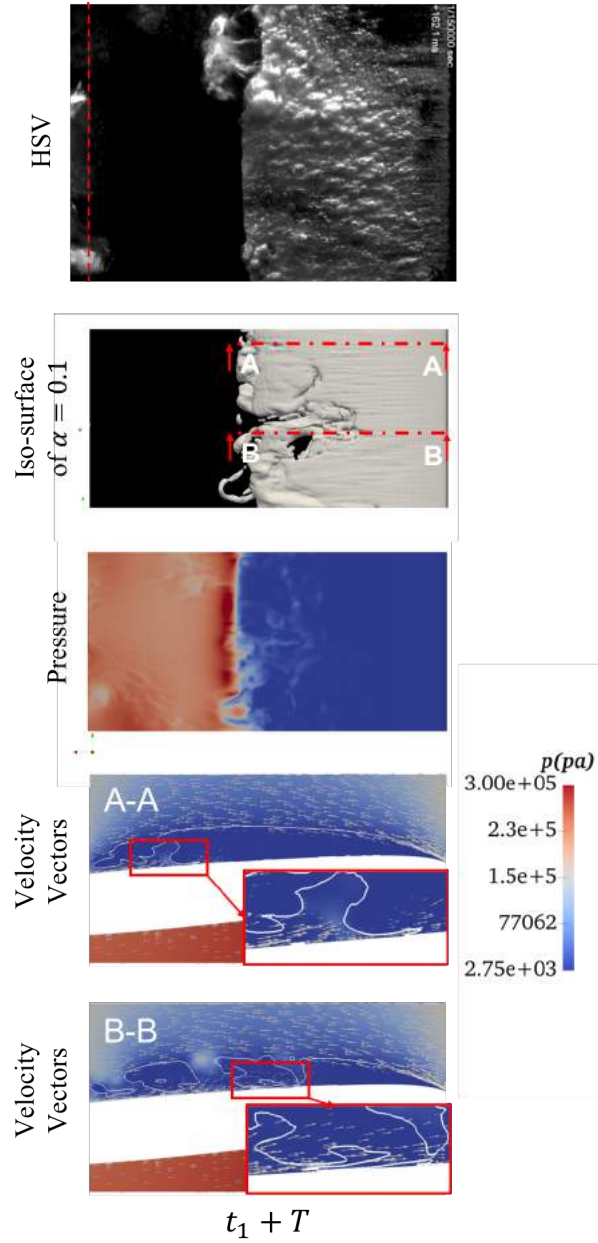


Figure 3.5: Delay in the formation of re-entrant jet 2

3.1.3 Correlation between stream-wise pressure gradient at closure line and re-entrant jet

In the explanation for the delay in the formation of re-entrant jet 2 and the creation mechanism of secondary re-entrant jet, it was argued that there is a strong correlation between the magnitude of stream-wise pressure gradient at the closure line and the strength and the initiation of these two re-entrant jets. For the re-entrant jet 2, the detachment of a vapour structure decreases the adverse pressure gradient and this delays the formation of the re-entrant jet 2 at the detachment location. For

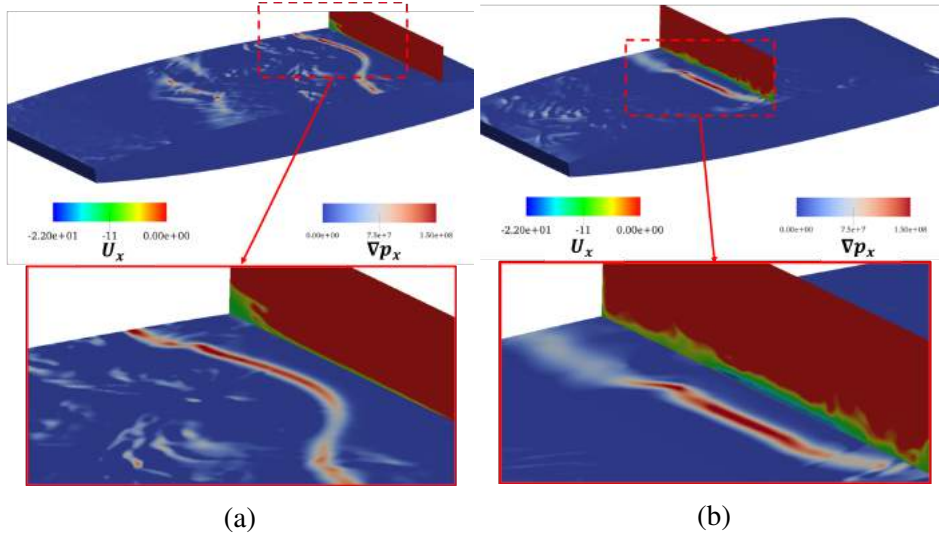


Figure 3.6: Stream-wise pressure gradient on the surface of the foil and the stream-wise velocity on a plane perpendicular to a) secondary re-entrant jet, b) re-entrant jet 2.

the secondary re-entrant jet, the collapse of some structures in the upstream part of the cloud cavitation increases the adverse pressure gradient at the closure line of the sheet cavity which in turn leads to the formation of the secondary re-entrant jet. In order to show this correlation, the stream-wise pressure gradient on the surface of the foil and the stream-wise velocity on a plane perpendicular to the re-entrant jet are shown for the instants corresponding to the initiation of re-entrant jet 2 and the secondary re-entrant jet. As it can be seen, in the regions where a strong stream-wise pressure gradient exists on the surface, the re-entrant jet has a higher negative value of stream-wise velocity which shows that the re-entrant jet is stronger in these regions. This observation is in line with the experimental studies by Laberteaux and Ceccio [61] and the numerical study by Gnanaskandan and Mahesh [62] which have shown that the adverse stream-wise pressure gradient at the closure line controls the strength of the re-entrant jet.

3.2 Secondary shedding

The secondary shedding is the detachment of vapour structures from the sheet and cloud cavities. Figure 3.7 shows the detachment of vapour structures related to the secondary shedding in HSV. Three type of cavity structures can be created in the secondary shedding.

- Cavity structures detached from the closure line of the sheet cavity due to its interaction with the re-entrant jet (vapour structure CS1 in figure 3.7a).
- Cavity structures detached from the sheet due to secondary re-entrant jet (vapour structure CS2 in figure 3.7b).

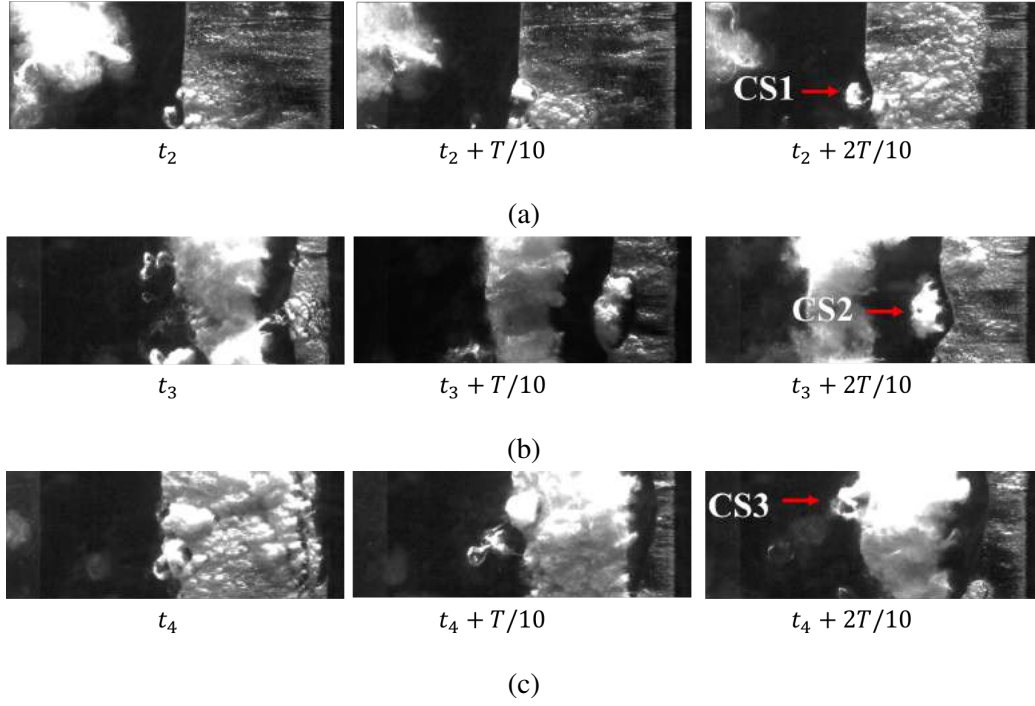


Figure 3.7: Detachment of vapour structures related to secondary shedding in HSV.

- Cavity structures detached from downstream end of the cloud cavity when it is rolling downstream (vapour structure CS3 in figure 3.7c).

As it will be shown later in this section, the numerical simulation with the current set-up and grid resolution can capture the secondary shedding, thus the numerical simulation results can be used to study the detachment process of the structures due to the secondary shedding in detail. The analysis of the flow details in the numerical simulation serves as a complementary tool to the limited information provided by HSV regarding the secondary shedding. Figure 3.8 presents the detachment process of the structure CS1 from the closure line of the sheet cavity in the numerical simulation. It can be seen in all instants that a region of high pressure can be seen at the closure line. The pressure difference between this region and the vapour pressure inside the sheet cavity creates a re-entrant flow which can be identified by the velocity vectors directed toward upstream. The interaction between re-entrant flow and the flow from upstream creates a vortex at the closure line which can be seen in the iso-surface of Q . At time t_2 , the closure line and the vortex at the closure line are almost two-dimensional. As time proceeds, the closure line and the vortex at the closure line start to become three-dimensional due to their interactions with the re-entrant jet. At time $t_2 + 6T/25$, the interaction between the re-entrant jet and closure line leads to the detachment of the structure CS1 from the sheet cavity. At this instant, the closure line is entirely three dimensional.

sional and the vortex at the closure line is broken into several three-dimensional structures. At time $t_2 + 9T/25$, the created vortical structure, CS1, has been lifted off from the surface and has been transformed into a horse-shoe shaped structure.

Figure 3.8 shows a strong correlation between vortical structures and cavitating structures. In order to study this correlation, the corresponding contours of vorticity components on C-C plane in figure 3.8 are depicted in figure 3.9. It can be clearly seen that when the sheet cavity has its maximum length at time t_2 , the vorticity is concentrated on the interface of the sheet cavity. This region of high vorticity is created due to the presence of a shear layer at the interface. The velocity inside the cavity is low while the velocity outside of the sheet cavity is of the same order as the inlet velocity. This velocity gradient creates a shear layer at the interface. The comparison between the contours of the three vorticity components indicates that the span-wise vorticity at time t_2 is larger than the other two components which means that the velocity gradient and the created shear layer are almost two-dimensional. As time proceeds, the shear layer becomes three-dimensional and the vorticity is distributed among the components uniformly in the closure line region. At time $t_2 + 9T/25$, the footage of the structure CS1 can be seen in the distribution of vorticity where a high vorticity can be detected in the head and legs of this structure. In order to identify which vorticity generation mechanism is responsible for transforming structure CS1 into a horse-shoe structure, the terms in the transport equation of stream-wise vorticity are analyzed. This equation reads as,

$$\frac{D\omega_x}{Dt} = \left[(\vec{\omega} \cdot \nabla) \vec{U} \right]_x - \left[\vec{\omega} (\nabla \cdot \vec{U}) \right]_x + \left[\frac{\nabla \rho_m \times \nabla p}{\rho_m^2} \right]_x + \left[\mathbf{v} (\nabla^2 \vec{\omega}) \right]_x, \quad (3.2)$$

where the terms in the right-hand side are, respectively, vortex stretching, vortex dilation, baroclinic term, and vortex dissipation term. Figure 3.9b shows the contour of these terms, except for the vortex dissipation term, on the C-C plane and at the corresponding instants in figure 3.8. The vortex stretching terms change the vorticity distribution by stretching the vorticity and tilting its orientation in the presence of the velocity gradient. For the stream-wise direction, the vortex stretching terms include $\omega_x \frac{\partial u_x}{\partial x}$, $\omega_y \frac{\partial u_x}{\partial y}$, and $\omega_z \frac{\partial u_x}{\partial z}$. At time t_2 , the magnitude of the vortex stretching terms are small as the two-dimensional velocity gradient at the interface of the sheet does not have the components in the span-wise direction, therefore $\omega_z \frac{\partial u_x}{\partial z}$ is almost zero. The other two terms, $\omega_x \frac{\partial u_x}{\partial x}$ and $\omega_y \frac{\partial u_x}{\partial y}$ are also small as the vorticity at time t_2 is mostly in span-wise direction (shown in figure 3.9). Once the velocity gradient at the interface become slightly three-dimensional at time $t_2 + 3T/25$ due to the disturbance created by the re-entrant jet, the vortex stretching terms becomes activated. It can also be seen that the vortex stretching terms increases around the structure CS1 as the vorticity and velocity gradient becomes more three-dimensional in this region. Similar trends can be observed in the distribution of vortex dilation terms. This term changes the stream-wise vorticity in the presence of velocity divergence which, in cavitating flows, occurs due to evaporation and condensation. At time t_2 , the vortex dilation

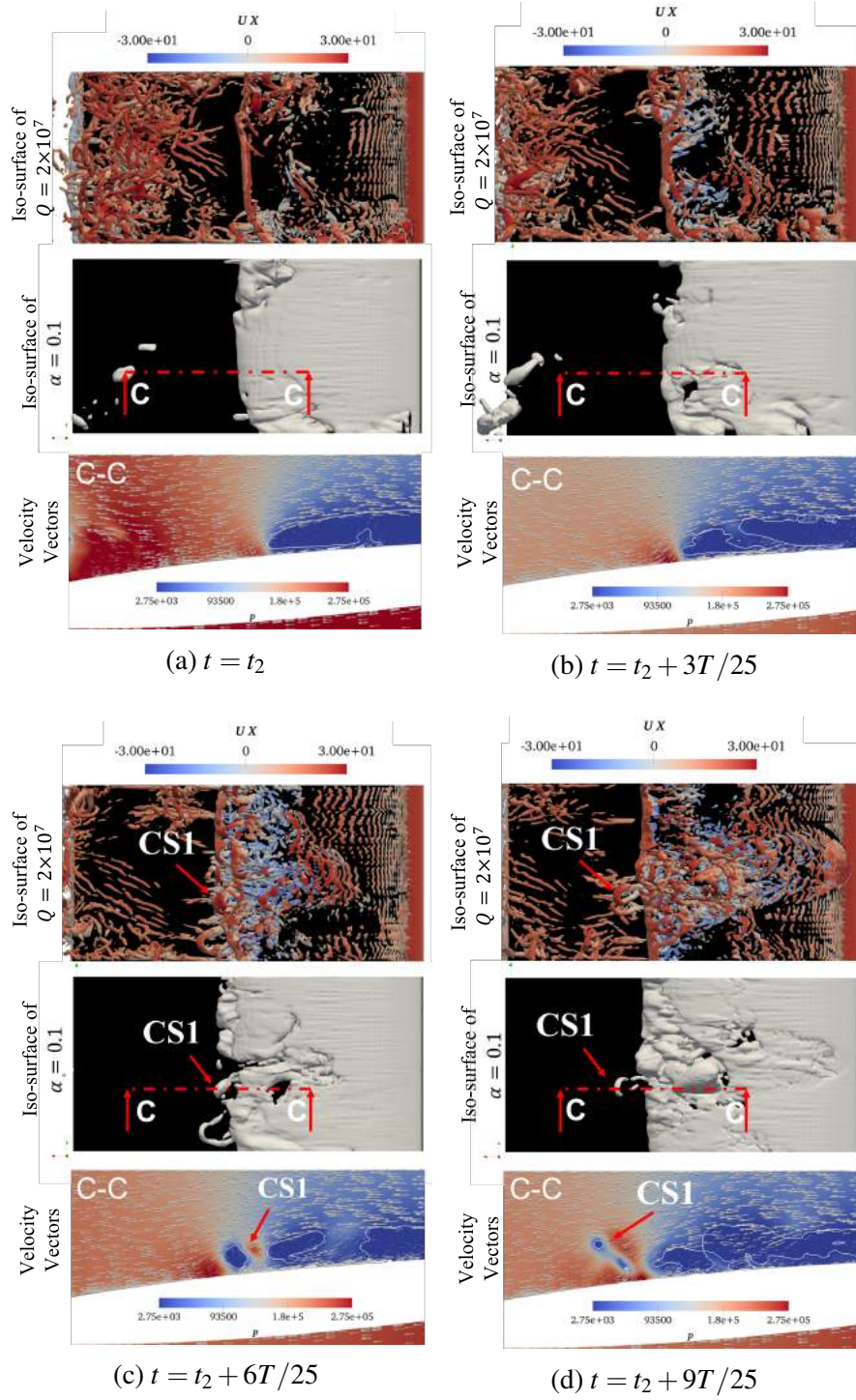


Figure 3.8: Detachment process of structure CS1 due to interaction between re-entrant jet and the closure line of the sheet cavity (Flow is from right to left).

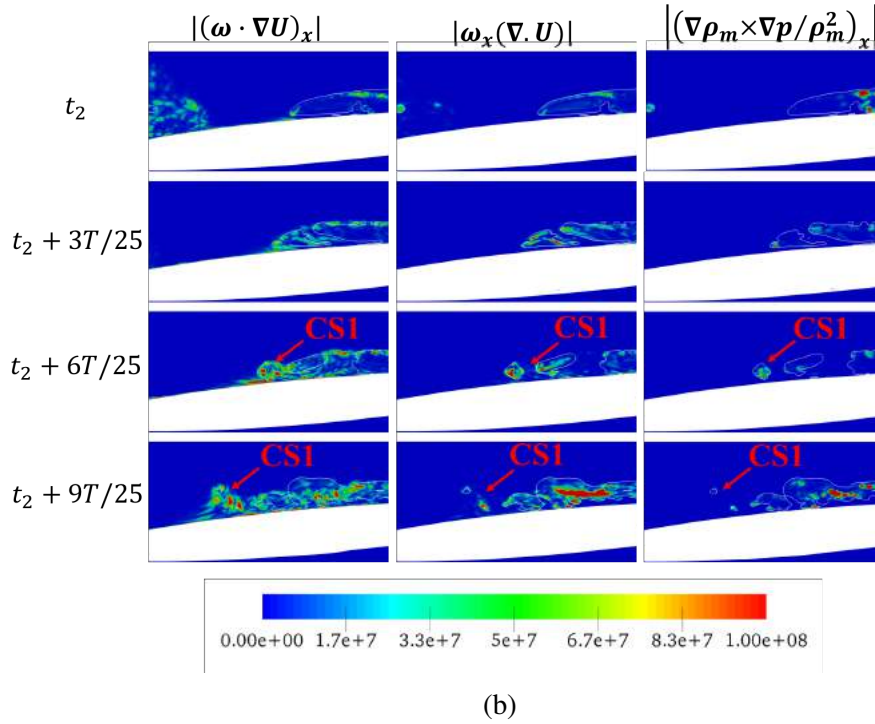
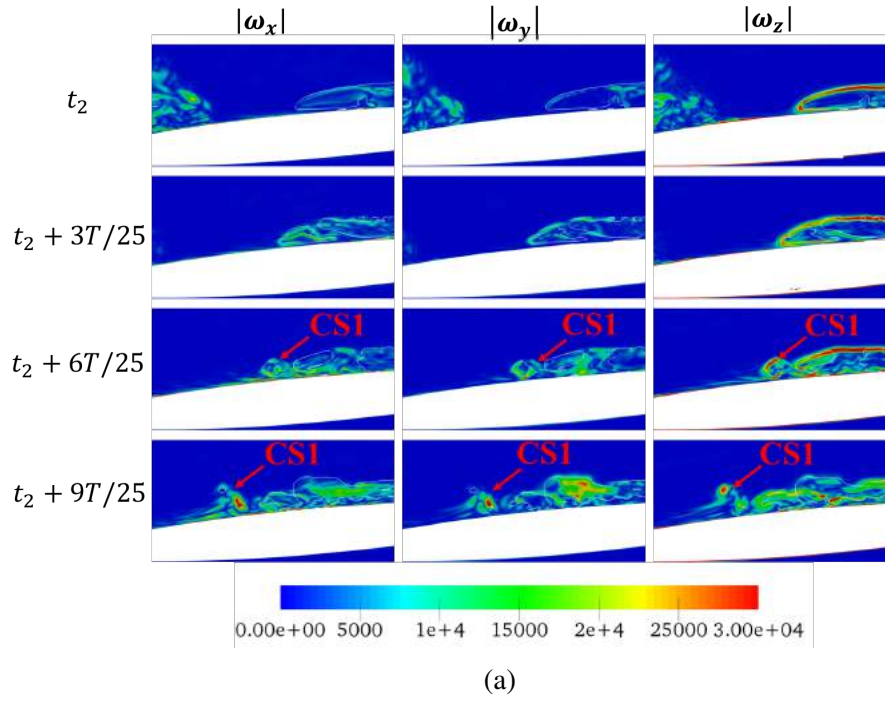


Figure 3.9: Analysis of vorticity components and terms in transport equation of stream-wise vorticity on C-C plane in figure 3.8, a) contours of vorticity components b) contours of the terms in transport equation of stream-wise vorticity.

terms are small as no evaporation or condensation occurs around the closure line. When the structure CS1 is detached from the closure line of the sheet cavity at time $t_2 + 6T/25$, this structure starts to collapse due to the high pressure at the closure line. This collapse induces a negative divergence of velocity which in turn magnifies the stream-wise vorticity through the vortex dilation term in the region around the structure CS1. It can also be seen that the baroclinic term, which is due to the non-alignment of pressure gradient and density gradient, is small around the closure line at time t_2 except for a small region on the interface. As time proceeds and the interface becomes disturbed by the re-entrant jet, the non-alignment of pressure and density gradient develops a component in the stream-wise direction which presents itself as a slight increase in the baroclinic term at time $t_2 + 9T/25$. However, the contribution of the baroclinic term to the increase of stream-wise vorticity in the region around the structure CS1 is small compared to the contribution of vortex stretching and vortex dilation terms; therefore it can be concluded that the vortex stretching and vortex dilation terms are the dominant vorticity generation mechanisms during the detachment process of the structure CS1.

Figure 3.10 presents the instants corresponding to the detachment of structure CS2 due to secondary re-entrant jet. At time t_3 , a new sheet cavity is formed and the cloud cavity is traveling downstream. The shear layer at the interface of the sheet cavity can be seen in the iso-surface of the Q criteria. At time $t_3 + T/7$, a secondary re-entrant jet is formed at the closure line of the sheet cavity. As mentioned in section 3.1, this re-entrant jet is due to a high pressure in the region between the upstream part of the cloud and the closure line of the sheet cavity. This high pressure can be seen at time $t_3 + T/7$. When this re-entrant jet hits the interface, it creates a disturbance on the interface of the sheet cavity. It can also be seen in the iso-surface of Q criteria at time $t_3 + T/7$ that the shear layer on the interface is broken into several three-dimensional structures as the shear layer interacts with the re-entrant jet. At time $t_3 + 2T/7$, the disturbance on the interface of the sheet cavity has grown and the three-dimensional vortical structures on the interface of the sheet cavity have rolled up and formed the structure CS2. It can be seen that the structure CS2 collapses at time $t_3 + 3T/7$ when it detaches from the closure line of the sheet cavity.

The corresponding contours of vorticity components on the D-D plane in figure 3.10 are presented in figure 3.11. At time t_3 , when a new sheet cavity is formed at the leading edge, the span-wise vorticity is a dominant component of vorticity. When the re-entrant jet hits the interface at time $t_3 + T/7$ and the interface of the sheet cavity becomes disturbed, the vorticity field around the interface of the sheet cavity develops components in the stream-wise and vertical directions. At instants $t_3 + 2T/7$ and $t_3 + 3T/7$, when the structure CS2 is detached from the sheet cavity, it can be seen that the vorticity at the location of structure CS2 is uniformly distributed between its components. To identify which vorticity mechanism is responsible for the formation of structure CS2, the contour of terms in the transport equation of stream-wise vorticity (equation 3.2) on plane C-C are plotted in figure 3.11b. At time t_3 , all terms on the right-hand side of equation 3.11b are small in

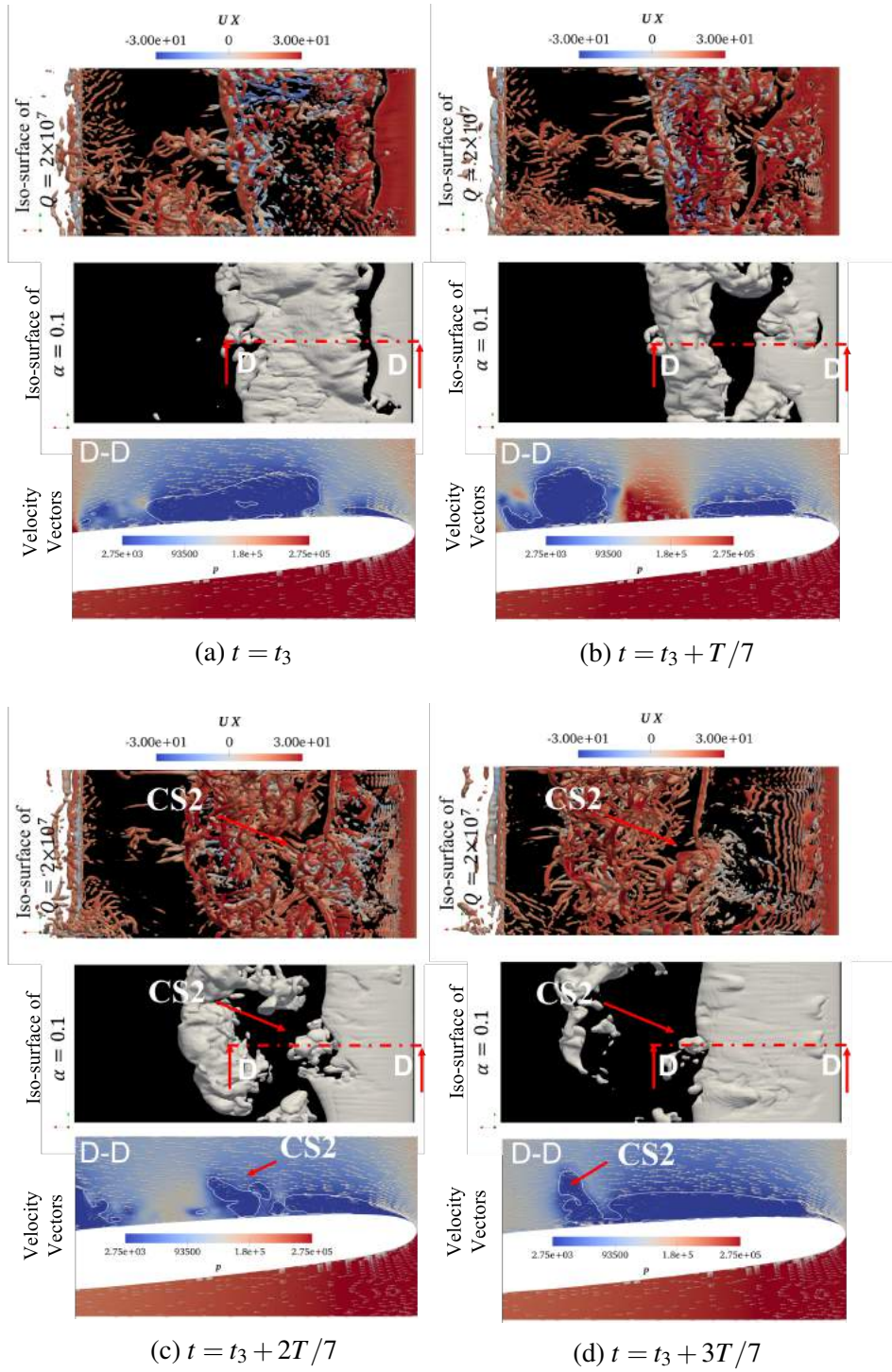
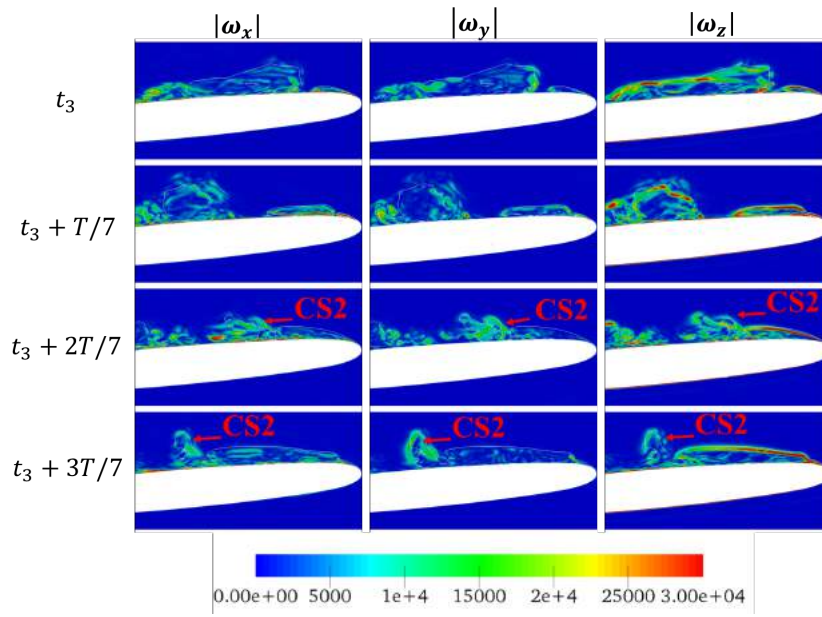
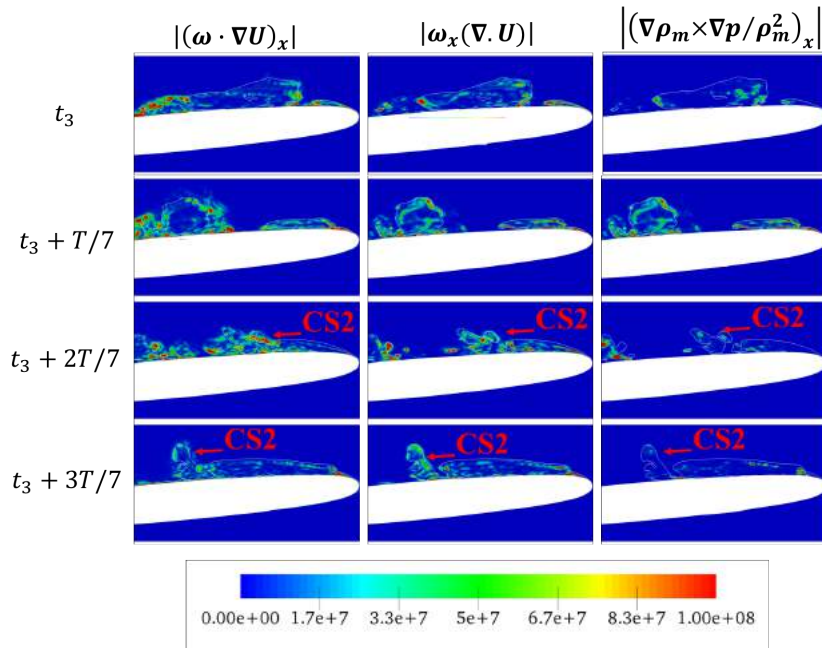


Figure 3.10: Detachment process of structure CS2 from the closure line of the sheet cavity due to the secondary re-entrant jet (Flow is from right to left).



(a)



(b)

Figure 3.11: Analysis of vorticity components and terms in transport equation of stream-wise vorticity on D-D plane in figure 3.10, a) contours of vorticity components, b) contours of the terms in transport equation of stream-wise vorticity.

the region where the newly formed sheet cavity is located. When the re-entrant jet interacts with the sheet cavity interface, the contributions of the three terms increases. As explained about the detachment process of the structure CS1, the interface of the sheet cavity and the velocity gradient on this interface become disturbed when the re-entrant jet interacts with the interface and this results in the activation of all vorticity mechanism. When the structure CS2 detaches from the closure line of the sheet cavity, it can be seen that the baroclinic term is negligible compared to the vortex stretching and vortex dilation terms which suggests that these two terms are the dominant vorticity transportation in the detachment process of structure CS2.

The detachment process of structure CS3 in the numerical simulation results is presented in figure 3.12. At time t_4 when the cloud cavity is detached from the leading edge, figure 3.12a shows that the upper surface of the cloud consists of several three-dimensional vortical structures. The origin of these structures is the same as the origin of the structure CS1, which is the shear layer on the interface of the sheet cavity. As mentioned in the description of the detachment process of structure CS1, the shear layer on the interface of the sheet cavity breaks into several three-dimensional cavitating vortical structures as this shear layer interacts with the re-entrant jet. These cavitating vortical structures then form the upper surface of the cloud when the cloud is detached from the leading edge. As time proceeds in figure 3.12, it can be seen that the structures in the downstream part of the cloud becomes larger. One possible explanation for this increase in size is that the structures in the upstream parts of the cloud merge together with the ones in the downstream part and form large vortical structure due to difference in stream-wise velocity in the upstream and downstream part of the cloud. This velocity difference can also be seen in the velocity vectors at plane D-D at time $t_4 + 2T/21$, where a low-velocity region can be detected around the downstream end of the cloud. It can also be observed that the structure CS3 is detached from the downstream end of the cloud at time $t_4 + 4T/21$ and it is collapsing at time $t_4 + 6T/21$. Figure 3.13 shows the contour of vorticity components on the plane E-E in figure 3.12. At time t_4 , the downstream end of the cloud corresponds to a high value of all vorticity components. The origin of this region of high vorticity is the velocity gradient at the interface of the sheet cavity, as explained before. It can also be seen that the span-wise component of vorticity in this region is slightly higher than the other two components. As time proceeds and the cloud cavity travels downstream, the vorticity becomes more uniformly distributed among the components. At instants $t_4 + 4T/21$ and $t_4 + 6T/21$, when the structure CS3 is detached from the downstream end of the cloud, all components of vorticity are high around the structure CS3. Figure 3.13b shows the terms in the transport equation of stream-wise vorticity on plane E-E. At time t_4 , it can be seen that the baroclinic term is negligible compared to the other two terms. As time proceeds, a slight increase in the baroclinic term can be seen. However, this term is still smaller than the vortex stretching and the vortex dilation terms, therefore the dominant terms during the detachment of structure CS3 are vortex stretching and vortex dilation.

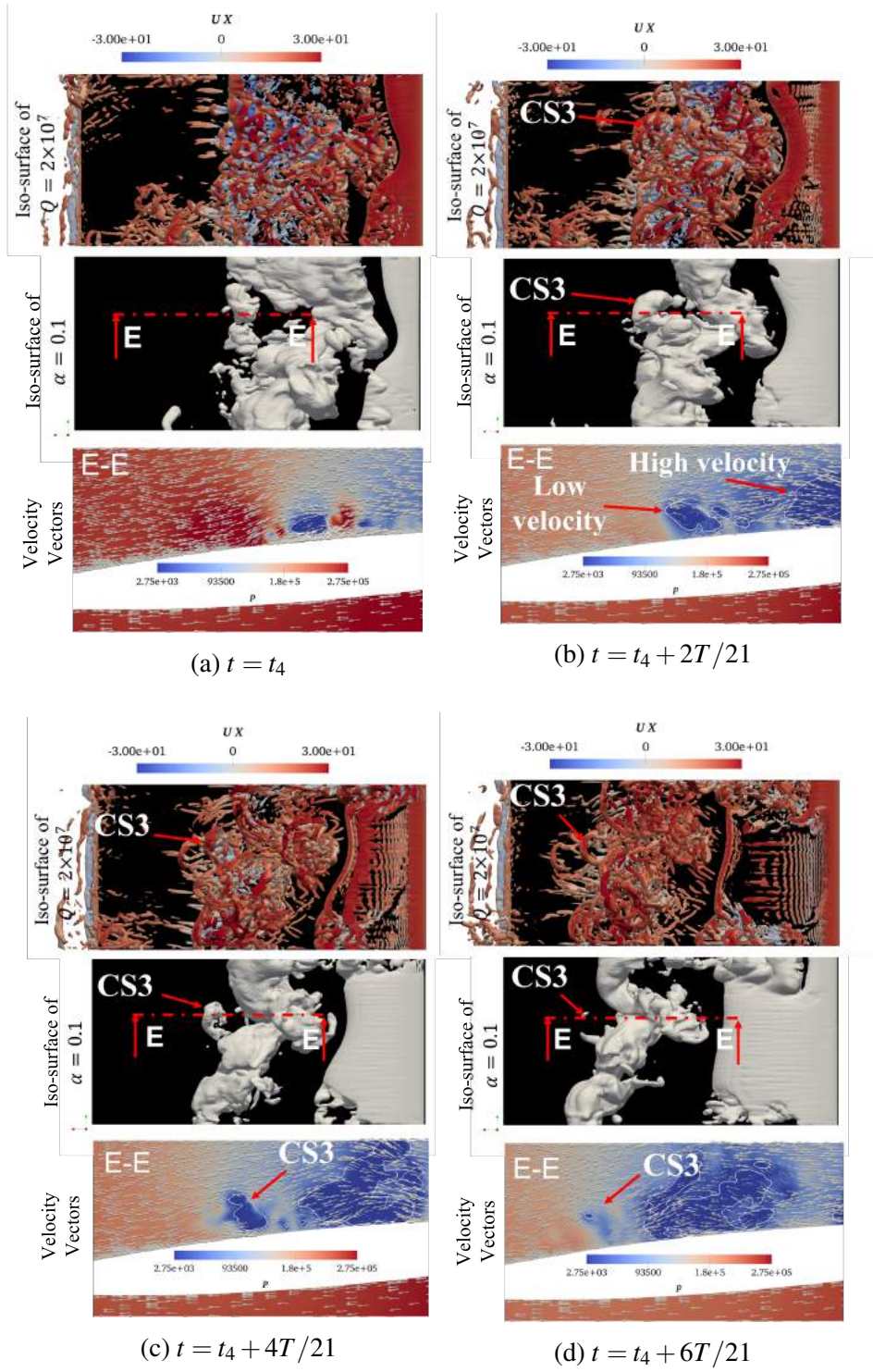


Figure 3.12: Detachment process of structure CS3 from downstream end of the cloud (Flow is from right to left).

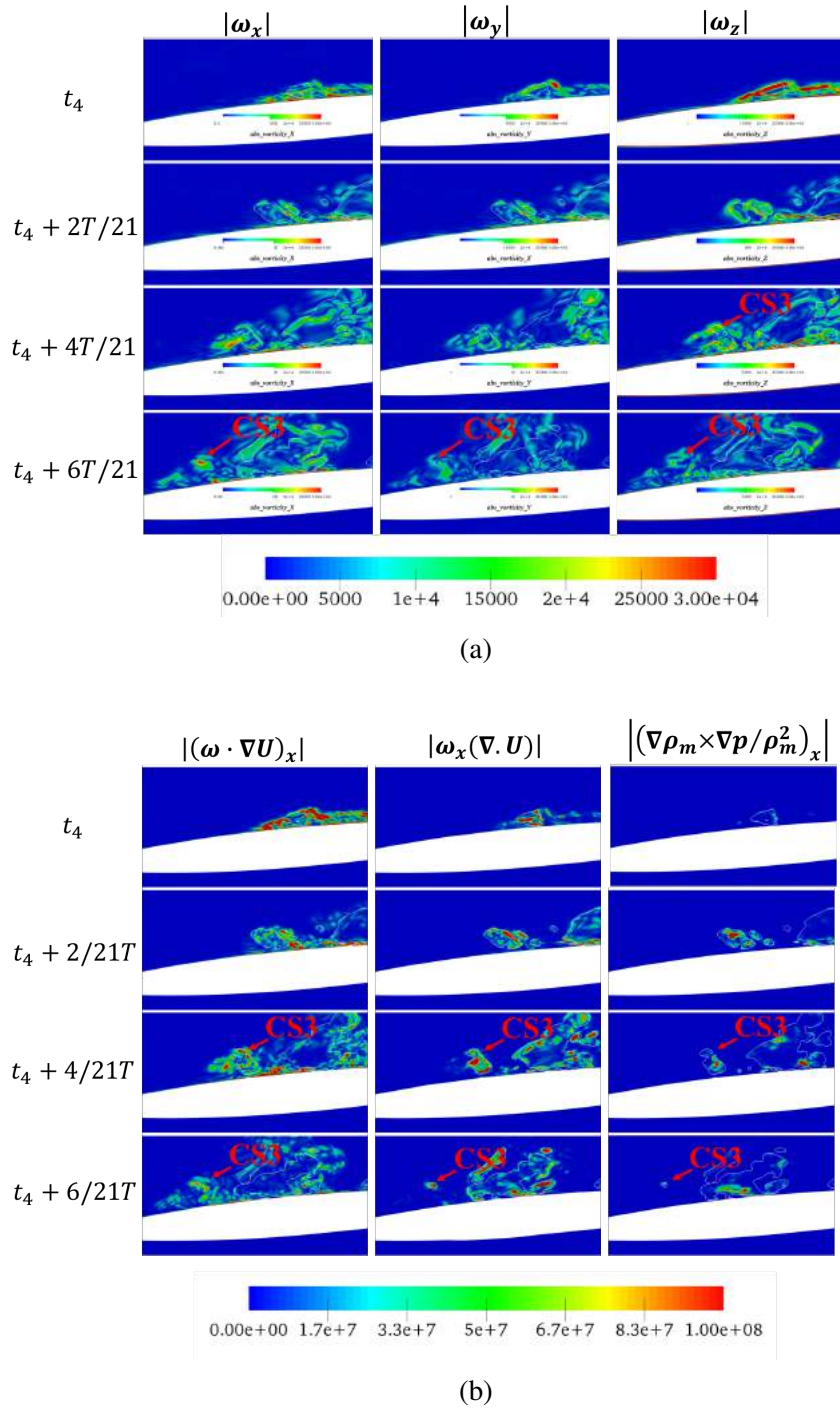


Figure 3.13: Analysis of vorticity components and terms in transport equation of stream-wise vorticity on E-E plane in figure 3.12, a) contours of vorticity components b) contours of the terms in transport equation of stream-wise vorticity.

3.3 Erosion assessment using paint test

In this section, the location of erosive collapses in the cavitating flows, of two cavitation numbers, are determined using a paint test method. Figure 3.14 shows the status of the paint layer after 15 minutes of cavitation test and span-wise average of the paint removal for two cavitation numbers. Four regions of paint removal can be observed in the paint test results. In two cases, a number of pits can be observed at the leading edge of the foil. The locations of these pits are marked as region 1 in figure 3.14. Region 2 is the paint removal around the stream-wise location equal to 60 percent of the sheet cavity maximum length. The third region is the paint removal around the closure line of the sheet cavity at its maximum length and the fourth region is a dispersed location of paint removal close to the trailing edge of the foil. In figure 3.14, it can also be seen that the maximum of paint removal in the case with $\sigma = 1.35$ and $\sigma = 1.25$ occurs around the closure line of the sheet cavity.

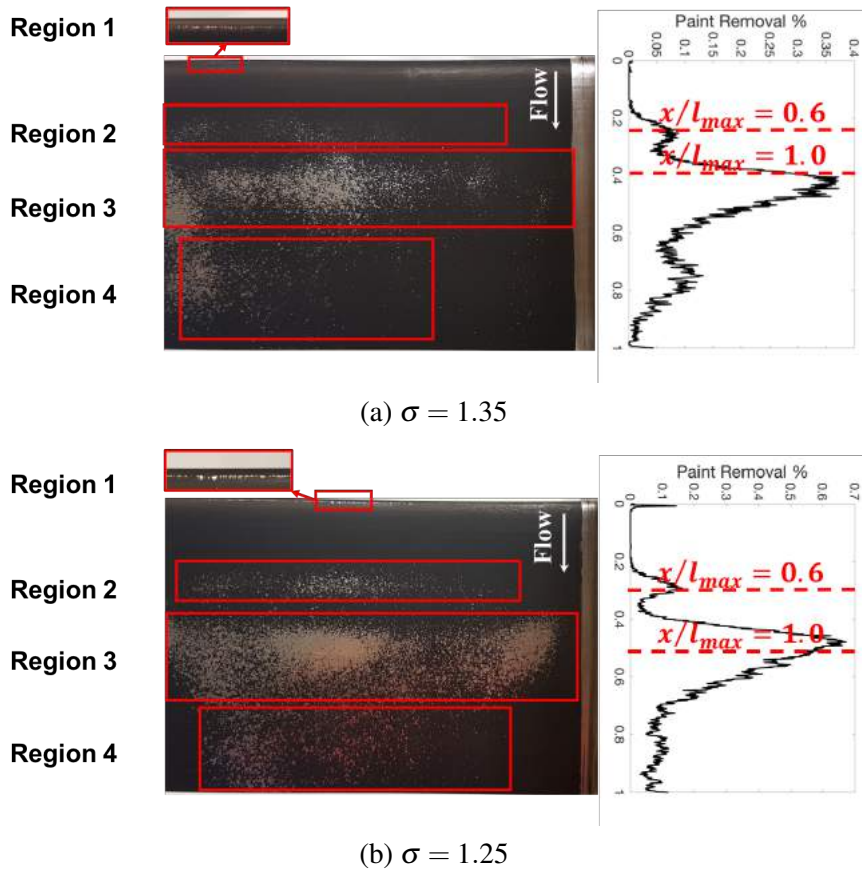


Figure 3.14: The paint removal after 15 min of cavitation test for different cavitation numbers (l_{max} : maximum length of the sheet cavity, x : stream-wise position from the leading edge).

3.4 On the relationship between cavitating structures and erosion patterns

In this section, the paint removal patterns in figure 3.14 and the detectable collapse events in the high-speed videos are used to find the relation between the erosion patterns and cavitation dynamics.

3.4.1 Collapse events in region 1

As it can be seen in figure 3.14, a region of paint removal is located on the leading edge of the foil. The location of these regions suggests that the collapse of the sheet cavity when the re-entrant jet hits the interface, shown in figure 3.15, is responsible for the paint removal in region 1.

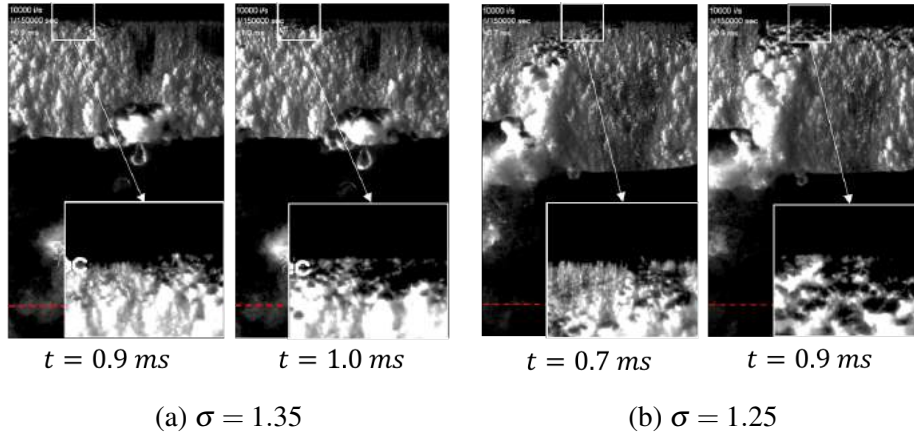


Figure 3.15: Collapse events in region 1 for different cavitation numbers (Flow is from top to bottom and the trailing edge is marked by a red dashed line).

3.4.2 Collapse events in region 2

Region 2 is the paint removal in the stream-wise location between the leading edge and the maximum length of the sheet cavity. According to HSV, the collapse of structures in the upstream part of a rolling cloud can be responsible for the paint removal in this region. Examples of these collapses in the two cavitating flows with different cavitation numbers are shown in figure 3.16. In these instants, the cloud cavity has been detached from the leading edge and a new sheet cavity is formed. The structures in the upstream part of the cloud cavity merge and form a cavitating vortex that can be observed in the second instant. Between the second and third instants, the created cavitating vortex collapses. As the collapse location of this cavitating vortex matches well with the location of the erosion pattern in region 2, it can be concluded that the collapse of this structure can be responsible for the erosion pattern in this region.

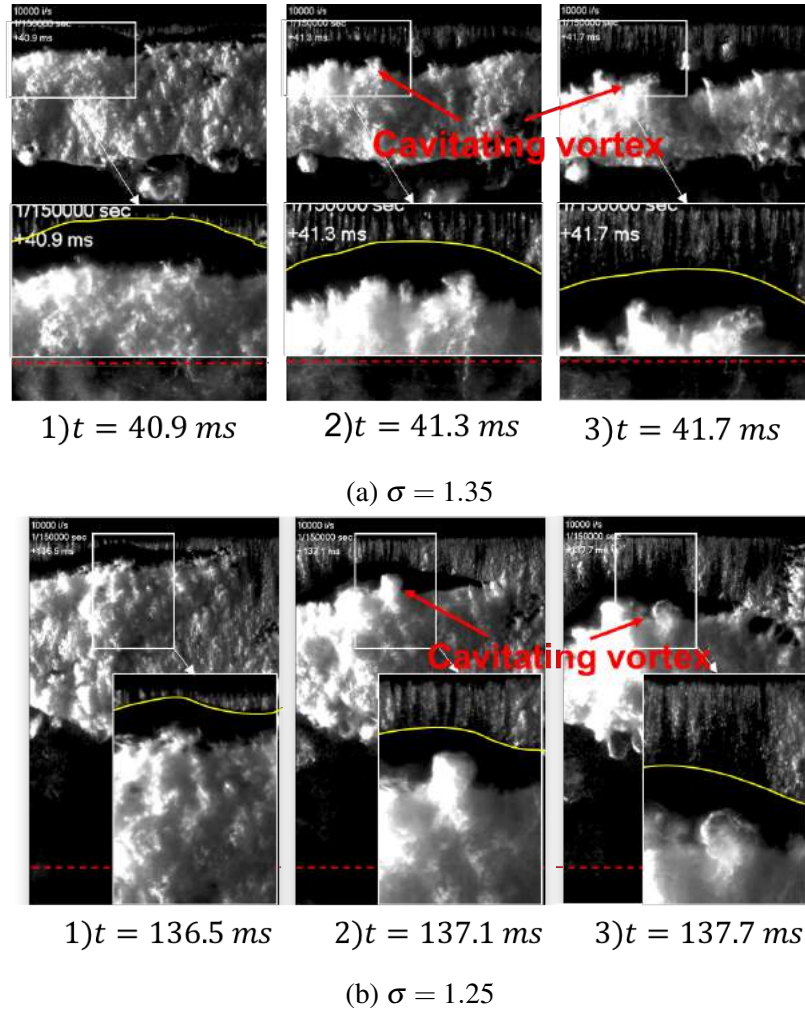


Figure 3.16: Collapse of small cavitating vortices in the upstream part of the cloud (Flow is from top to bottom and the trailing edge is marked by a red dashed line).

3.4.3 Collapse events in region 3

In figure 3.14, region 3 is the paint removal around the closure line of the sheet cavity when it reaches its maximum length. In HSV, several collapse events can be detected in this region. The first type of collapse events here is the collapse of small structures in downstream end of the cloud when it is rolling downstream. Figure 3.17 shows the instants related to this type of collapse events. As it can be seen, small structures detach from the downstream end of the cloud and collapse shortly after their detachment. The detachment process of these structures is one mechanism of secondary shedding as explained in section 3.2 using numerical simulation results. Another type of collapse events which occurs around the paint removal in region 3 is the collapse of large vortical cavity structures in the cloud cavity, shown in figure 3.18. In these instants, the structures in the upstream

part of the cloud have merged into a large cavitating vortex similar to figure 3.16. However, the created vortex here is larger compared to the one in figure 3.16. This difference can be one possible explanation for the difference in the collapse location of the cavitating vortices in figures 3.18 and 3.16. As the cavitating vortex in figure 3.18 is larger, it has a larger collapse time if we assume that both cavitating vortices are subjected to the same outside pressure. Therefore, the larger cavitating vortices can be transported further downstream before the collapse compared the one in figure 3.16.

Another example of collapse events in region 3 is the collapse of vapour structures detached from the closure line of the sheet cavity. Figure 3.19 presents the process related to this type of collapse events at the two cavitation numbers. In the first instants, a disturbance can be seen in the interface of the sheet cavity. This disturbance is created by the interaction between the second re-entrant jet in figure

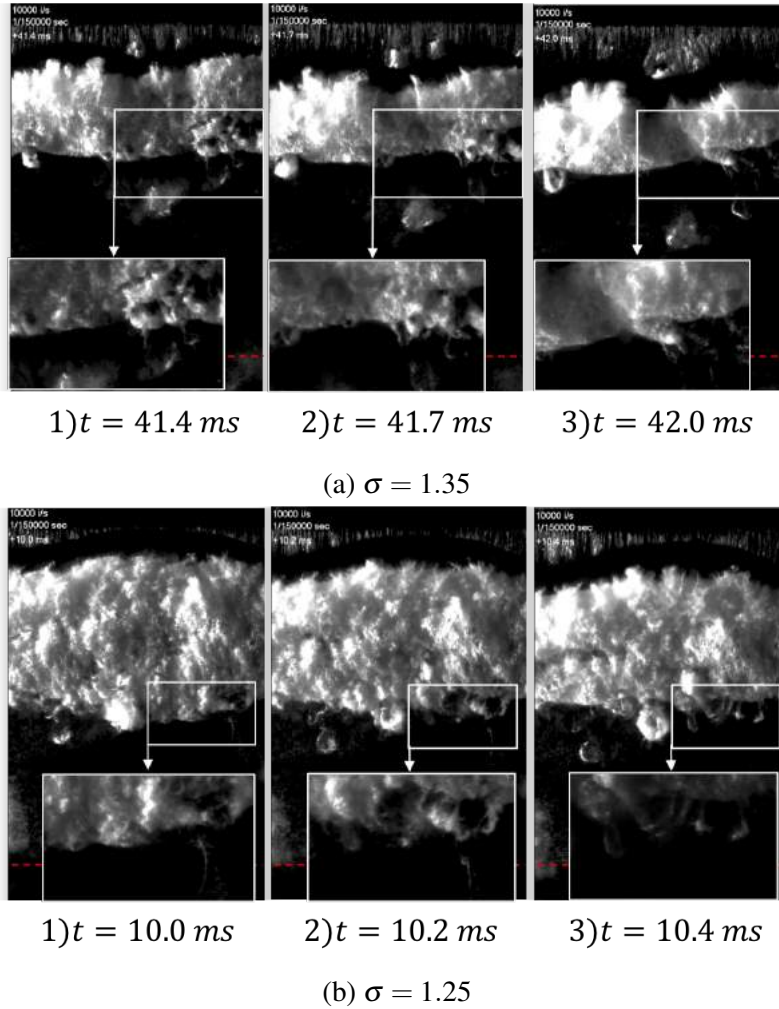


Figure 3.17: Collapse of structures in downstream end of rolling cloud (Flow is from top to bottom and the trailing edge is marked by a red dashed line).

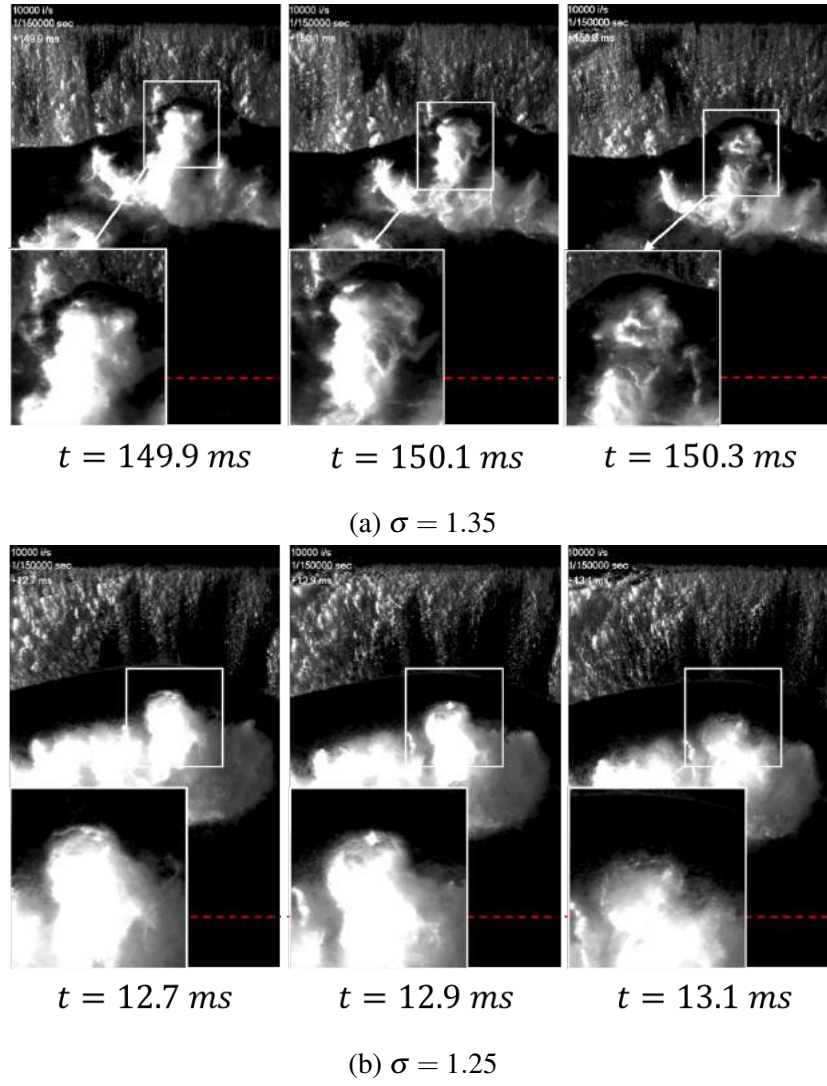


Figure 3.18: Collapse of large cavitating vortex in upstream part of the cloud (Flow is from top to bottom and the trailing edge is marked by a red dashed line).

3.4 and the interface of the sheet cavity. This disturbance becomes larger as the sheet cavity grows. In the second instant, a cavity structure is detached from the closure line of the sheet cavity and transforms into a horse-shoe vortical structure. These vortical structures collapse shortly after their detachment, possibly due to high pressure in the closure line of the sheet cavity.

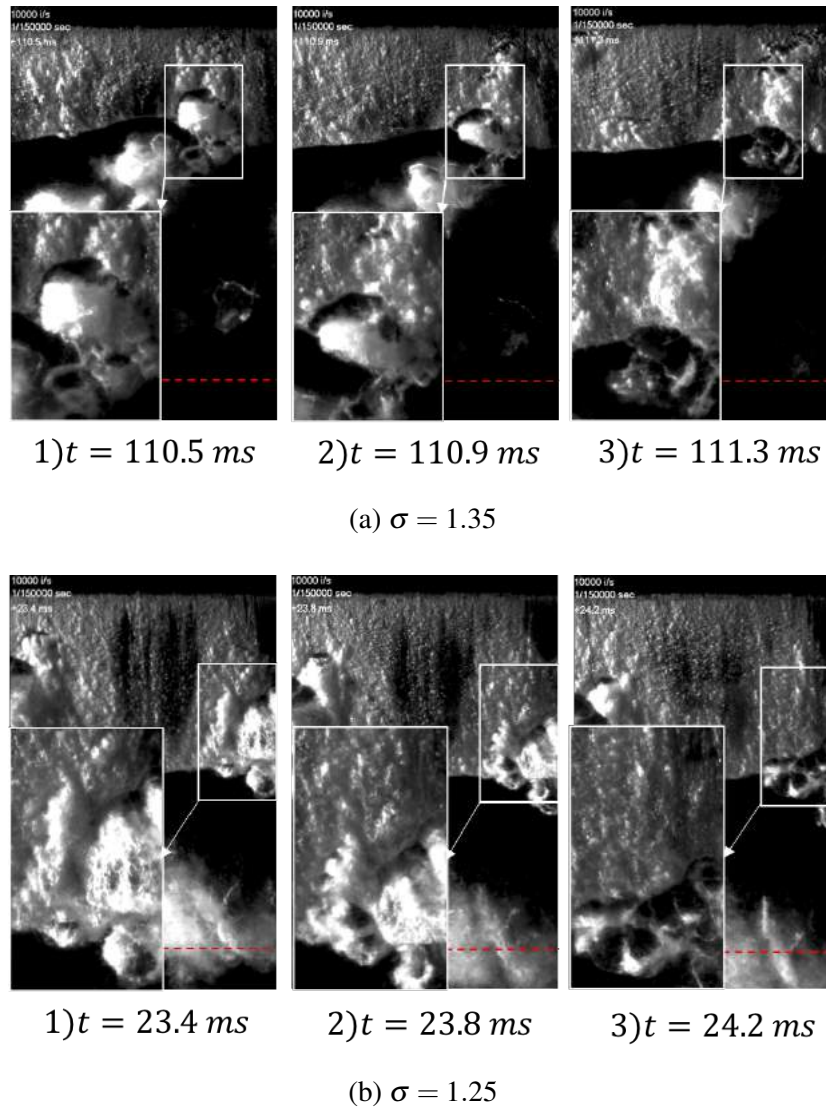


Figure 3.19: Collapse of horse-shoe vortical structures detached from the closure line of the sheet cavity (Flow is from top to bottom and the trailing edge is marked by a red dashed line).

3.4.4 Collapse events in region 4

In the two erosion patterns in figure 3.14, region 4 is a dispersed paint removal close to the trailing edge of the foil. HSV suggests that the paint removal in this region is created by the large scale collapse of the cloud shed due to primary shedding. Figure 3.20 shows the examples of this collapse at the two cavitation numbers. In these images, the cloud cavity is detached from the leading edge and is transported by the flow into the high pressure region near the trailing edge. Due to this high pressure, the large scale structures in the cloud collapse in the paint removal region.

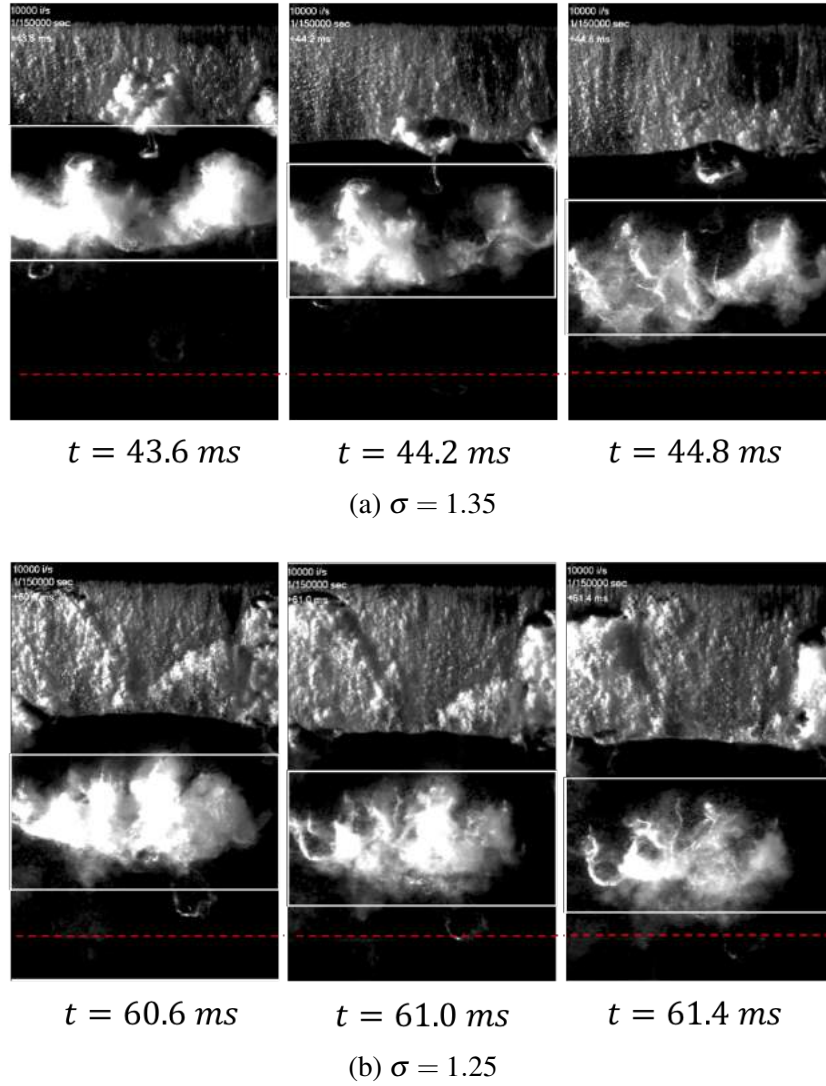


Figure 3.20: Collapse of the large scale cloud cavities close to the trailing edge of foil (Flow is from top to bottom and the trailing edge is marked by a red dashed line).

3.5 Erosion assessment using compressible solver

In order to numerically assess the areas with high risk of cavitation erosion, the cavitating flow at $\sigma = 1.25$ is simulated using the compressible solver with the inviscid barotropic cavitation model. Figure 3.21 shows the comparison between the cavitation dynamics in one cycle in the results from the compressible solver and high-speed videos. As it can be seen, the compressible inviscid solver is capable of reproducing the main behavior of the cavitating flow. It is also noted that the maximum length of the sheet cavity in the simulation results at time $t = t_1$ and $t = t_1 + T$ is slightly shorter than the length of the sheet cavity in HSV. Figure 3.22a shows the maximum recorded pressure on the surface of the foil and figure

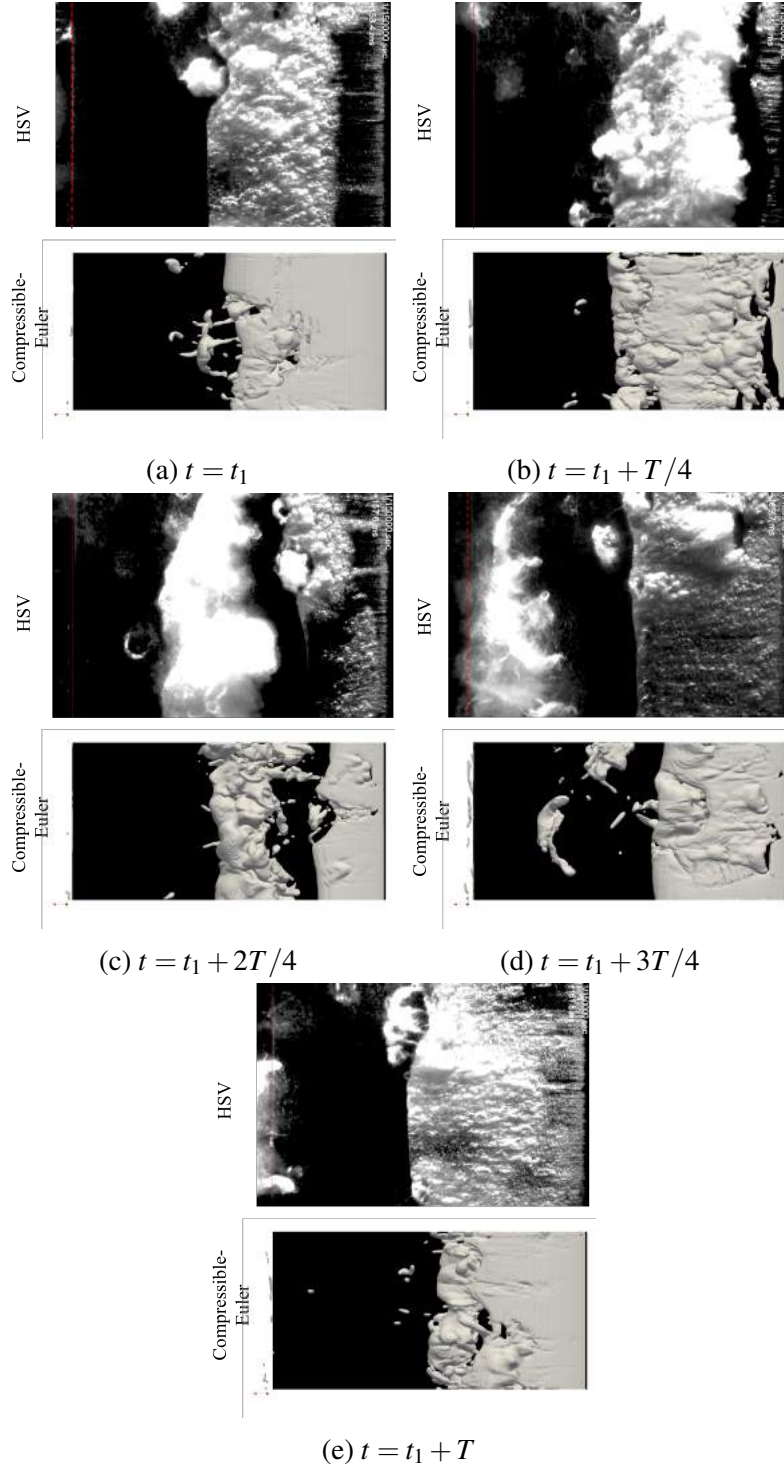


Figure 3.21: Comparison between primary shedding in HSV and compressible simulation results for the cavitating flow with $\sigma = 1.25$ (Flow is from right to left and the trailing edge is marked by a red dashed line).

3.22b presents the collapse locations with the maximum pressure larger than 60 bars during the compressible simulation. The comparison between the results in figure 3.22 and the paint test results in figure 3.14b shows that regions of high maximum surface pressure and the collapse locations are qualitatively in good agreement with the erosion pattern obtained by the paint test. Similar to the paint test results, four regions can be identified in figure 3.22. Region 1, which is related to the collapse of sheet cavity is well predicted by numerical simulation results. The predicted pressure pulses and the collapse points in region 2 are more spread out compared to paint removal of region 2 in figure 3.14b. This discrepancy can be due to that the effect of side walls are not present in the simulation. In the experiment, the presence of the wall concentrates the erosive collapses of region 2 in the mid-span location but as the effect of the side walls are ignored in the simulations, the predicted collapse points in different cycles can occur in different span-wise location. Another discrepancy between the location of predicted erosive collapses and the paint test is related to the location of regions 2, 3 and 4 as these locations are slightly shifted upstream compared to the paint test. This can be due to the shorter sheet cavity in the compressible simulation compared to the sheet cavity in HSV, as shown in figure 3.21. Another reason for this discrepancy can be the equilibrium assumption in the compressible solver. Because of this assumption, the condensation in the rolling cloud is assumed to occur instantaneously when the pressure is higher than vapour pressure. However, the collapse of clouds in the experiment might not be instantaneous and non-equilibrium effects might be present. Therefore, the clouds in numerical simulation collapse earlier compared to the experiment and the predicted collapse points are closer to the leading edge as compared to the paint test.

The results from the compressible solver are used to investigate the hydrodynamic mechanisms of erosive collapses. The erosive collapse can be divided into two groups based on their hydrodynamic mechanisms, the collapse events related to the structures in the sheet cavity and the collapse events related to the structures in the cloud cavity. Figure 3.23 shows the instants when the collapse of structures in the sheet cavity induces a pressure pulse larger than 60 bars on the surface of the foil. In figure 3.23a, the re-entrant jet has reached the leading edge and has detached a part of sheet cavity from the surface. The small part of the sheet cavity that remains on the leading edge collapses and produces a pressure pulse on the leading edge. As mentioned earlier, this collapse event is responsible for the paint removal of region 1 in figure 3.14b. In figure 3.23a and 3.23b, it can also be seen that while the sheet cavity has reached the maximum length, a high pressure pulse is detected on the surface around the closure line of the sheet cavity. As described in section 3.2, small vapour structures are detached from the closure line of the sheet cavity when the closure line interacts with the re-entrant jet. The collapse of these small vapour structures creates high pressure on the surface and are responsible for the paint removal of region 3 in figure 3.14b.

Figure 3.24 shows the instants when large pressure pulses due to the collapse of structures in the cloud are detected on the surface. In figure 3.24, the cloud

cavity is detached from the sheet cavity and rolls downstream. Figure 3.24a shows the instant when a structure in the upstream part of the rolling cloud collapses and produces high pressure on the surface. The location of this collapse event suggests that this collapse is responsible for the paint removal of region 2 in figure 3.14b. Figure 3.24a and 3.24b show that small structures in the downstream end of the

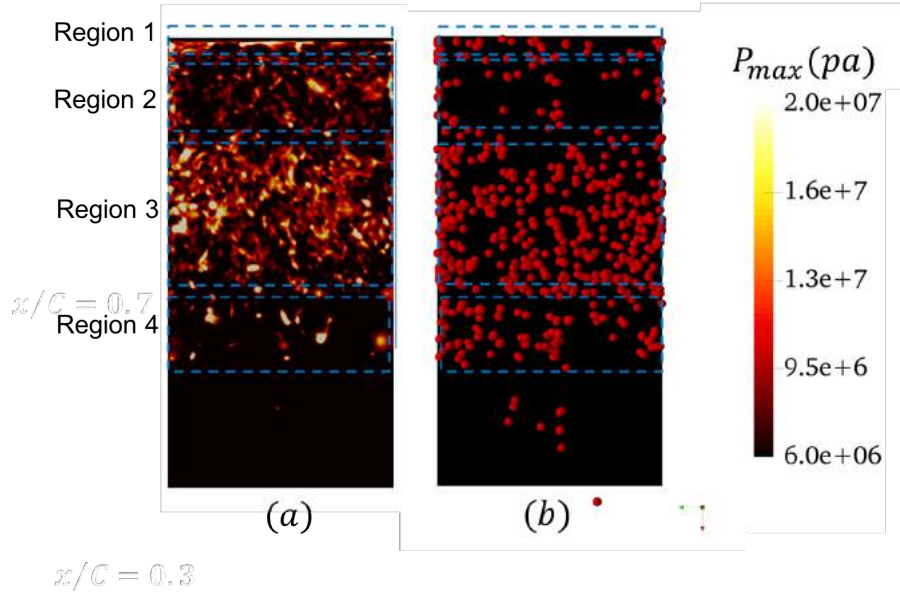


Figure 3.22: Erosion assessment using compressible solver, a) Maximum recorded pressure on each face of the surface, b) spatial distribution of collapse points with pressure higher than 60 bar (each sphere represents a collapse point) (Flow is from top to bottom).

cloud and structures underneath of the cloud collapse and produce high pressure pulse on the surface. These collapse events are the mechanism of paint removal in region 2 in figure 3.14b. In figure 3.24c, it can be seen that a large part of the cloud cavity collapses as it travels downstream and this collapse event produces a large pressure pulse on the surface of the foil. These collapse events are responsible for paint removal in region 4 in figure 3.14b.

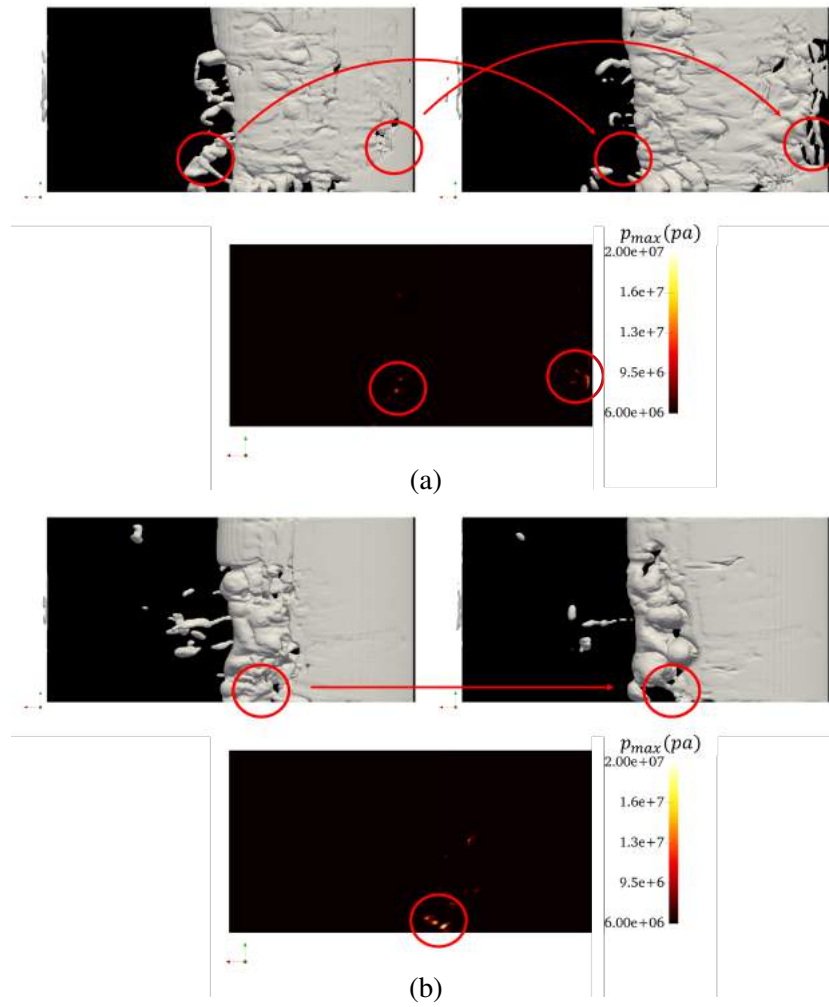


Figure 3.23: Instants when the collapse of structures related to the sheet cavity induces pressure pulse large than 60 bars on the surface (Flow is from right to left).

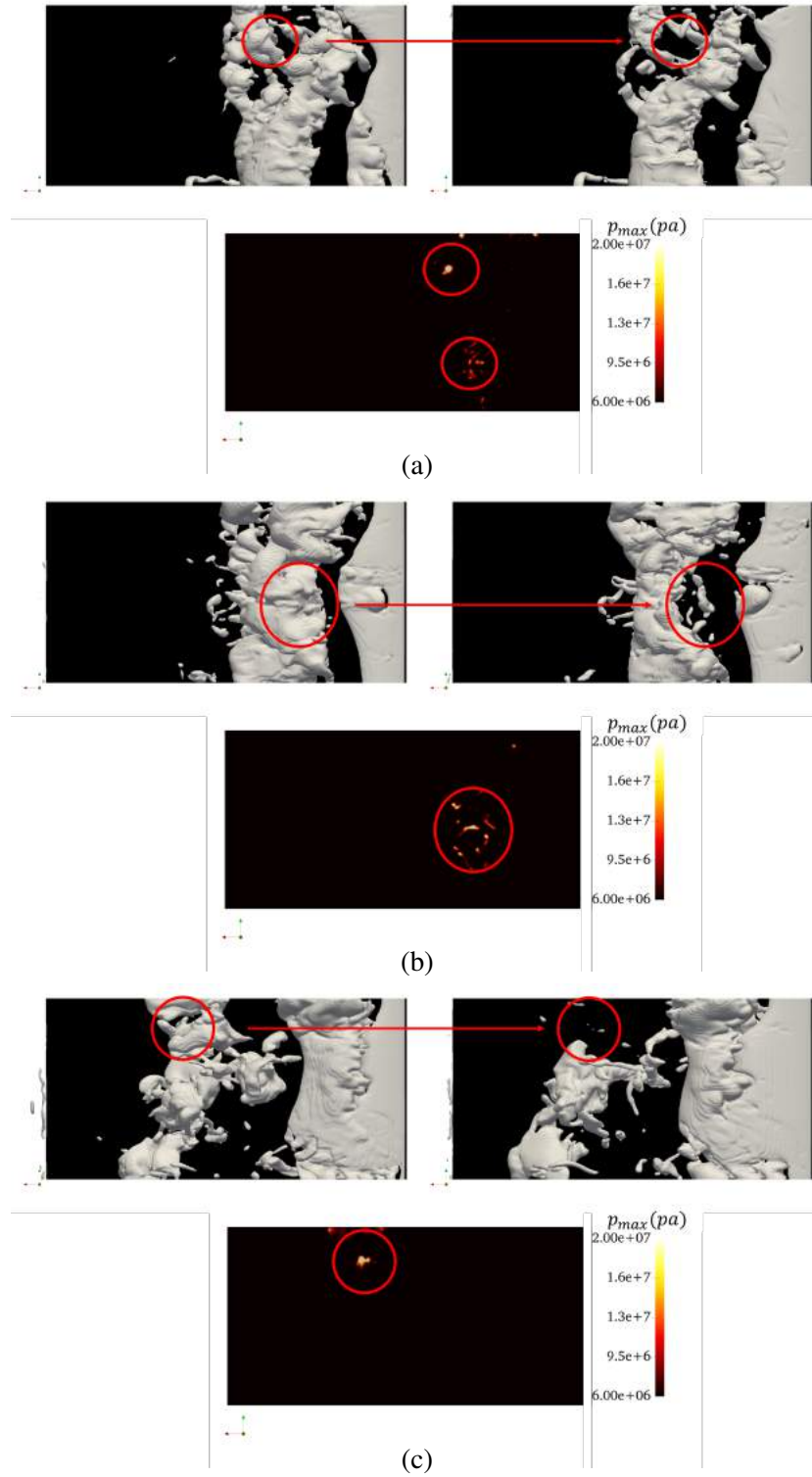


Figure 3.24: Instants when the collapse of structures related to the cloud cavity induces pressure pulse large than 60 bars on the surface (Flow is from right to left).

4

Conclusions

In this thesis, cavitating flows over a NACA0009 foil are studied using experimental and numerical methods. The following conclusion can be made based on the investigation in this thesis.

- The high-speed videos and numerical simulation results show that the cavitation dynamics in the cavitating flows studied here are controlled by two types of shedding, primary shedding and secondary shedding.
- The primary shedding is the shedding of large-scale cloud cavity from the leading edge due to re-entrant jet. A detailed analysis of this type of shedding in high-speed videos and numerical simulation results reveals the presence of the secondary re-entrant jet in each cycle. In contrast to the main re-entrant jet, which develops at the closure of the sheet cavity at its maximum length, this secondary re-entrant jet is formed when the sheet cavity is growing. The analysis of high-speed videos and the numerical simulation results suggest that this re-entrant jet is due to high pressure in the region between the upstream part of the cloud and closure line of the sheet cavity. This secondary re-entrant jet creates a disturbance on the interface of the sheet cavity when it reaches the leading edge. When this disturbance reaches the closure line, it delays the formation of the re-entrant jet in the next cycle in the region of this disturbance. This delayed re-entrant jet can lead to a very complex shedding behavior which can be seen in high-speed videos.
- The secondary shedding is the detachment of small-scale cavity structures from the sheet cavity and downstream end of the cloud cavity. Three types of cavity structure can be created in this type of shedding. The first type is the cavity structures detached due to the interaction between the closure line and the re-entrant jet. Due to this interaction, cavitating vortical structures are shed from the closure line and transformed into a horse-shoe shape

mostly by vortex stretching and vortex dilation mechanisms. The second type of structures in the secondary shedding is cavities separated from the closure line due to secondary re-entrant jet. These cavities are created at the location of the disturbance caused by secondary re-entrant jet or delayed main re-entrant jet. The third type of cavity structures in secondary shedding is small horse-shoe cavities shed from the downstream end of the cloud. Based on the numerical simulation results, these structures are created when the vortical structures at the downstream end of the cloud grow in size. The formed structure is then detached from the downstream end of the cloud and collapses shortly after its detachment.

- Based on the paint test results, four regions with a high risk of cavitation erosion are identified. The first region is located on the leading of the foil and high-speed videos show that the high risk of erosion in this region is due to the collapse of the remaining part of the sheet cavity on the leading edge. The second region is located around stream-wise location equal to 60 percent of maximum length the sheet cavity. Analysis of high-speed videos in this region shows that the collapse of small vortical structures in the upstream part of the cloud are responsible for the high risk of cavitation erosion in this region. The third region with a high risk of cavitation erosion occurs around the closure line of the sheet cavity at its maximum length. High-speed videos show that the collapse of structures detached due to secondary shedding, and the collapse of large cavitating vortical structures in the upstream part of the cloud can be detected in this region. The fourth region with high erosion risk is the region close to the trailing edge. The high risk of erosion in this region is due to the collapse of large-scale cloud cavity shed due to the primary shedding according to high-speed videos.
- The maximum recorded pressure on the surface of the foil and collapse locations with the maximum pressure larger than 60 bars obtained by the compressible simulation are used to numerically identify the areas with high risk of cavitation erosion. The comparison between results from the compressible simulation and paint test shows that regions of high maximum surface pressure and the collapse locations are qualitatively in good agreement with the erosion pattern obtained by the paint test. Erosive collapse events in the compressible simulation are analyzed to identify the hydrodynamic mechanisms of these events. These mechanisms are the collapse of the remaining part of the sheet cavity on the leading edge, the collapse of structures around the closure line of the sheet cavity, the collapse of small structures around and underneath of the cloud when it rolls downstream and the collapse of large-scale cloud close to the trailing edge.

REFERENCES

- [1] H. Lee, A. Gojani, T. Han, and J. Yoh. Dynamics of laser-induced bubble collapse visualized by time-resolved optical shadowgraph. *Journal of Visualization*, 14(4): 331–337, 2011.
- [2] S. Fujikawa and T. Akamatsu. Effects of the non-equilibrium condensation of vapour on the pressure wave produced by the collapse of a bubble in a liquid. *Journal of Fluid Mechanics*, 97(3):481–512, 1980.
- [3] M. Plesset and R.B. Chapman. Collapse of an initially spherical vapour cavity in the neighbourhood of a solid boundary. *Journal of Fluid Mechanics*, 47(2):283–290, 1971.
- [4] G. Bark, M. Grekula, R. Bensow, and N. Berchiche. On some physics to consider in numerical simulation of erosive cavitation. In *7th International Symposium on Cavitation, Michigan, USA*, 2009.
- [5] G. Bark, M. Grekula, and N. X. Lu. Analysis of erosive cavitation by high speed video records. In *Proceedings of the 2nd International Conference on Advanced Model Measurement Technology for the EU Maritime Industry, UK*, 2011.
- [6] G. Bark and R.E. Bensow. Hydrodynamic mechanisms controlling cavitation erosion. *International Shipbuilding Progress*, 60(1-4):345–374, 2013.
- [7] M. Dular and M. Petkovšek. On the mechanisms of cavitation erosion—coupling high speed videos to damage patterns. *Experimental Thermal and Fluid Science*, 68:359–370, 2015.
- [8] M. Petkovšek and M. Dular. Simultaneous observation of cavitation structures and cavitation erosion. *Wear*, 300(1-2):55–64, 2013.
- [9] M. Van Rijsbergen, E. Foeth, P. Fitzsimmons, and A. Boorsma. High-speed video observations and acoustic-Impact measurements on a NACA0015 foil. In *Proceedings of the 8th International Symposium on Cavitation, Singapore*, 2012.

- [10] Y. Cao, X. Peng, K. Yan, L. Xu, and L. Shu. A qualitative study on the relationship between cavitation structure and erosion region around a 3d twisted hydrofoil by painting method. In *Fifth International Symposium on Marine Propulsors, Finland*, 2017.
- [11] M. Callenaere, J. Franc, J. Michel, and M. Riondet. The cavitation instability induced by the development of a re-entrant jet. *Journal of Fluid Mechanics*, 444: 223–256, 2001.
- [12] T. Liu, B. Khoo, and W. Xie. Isentropic one-fluid modelling of unsteady cavitating flow. *Journal of Computational Physics*, 201(1):80–108, 2004.
- [13] C.E. Brennen. *Fundamentals of multiphase flow*. Cambridge university press, 2005.
- [14] J. Franc and J. Michel. *Fundamentals of cavitation*, volume 76. Springer Science & Business Media, 2006.
- [15] R. Fortes-Patella, G. Challier, J. Reboud, and A. Archer. Energy balance in cavitation erosion: from bubble collapse to indentation of material surface. *Journal of Fluids Engineering*, 135(1):011303, 2013.
- [16] E. Johnsen and T. Colonius. Numerical simulations of non-spherical bubble collapse. *Journal of Fluid Mechanics*, 629:231–262, 2009.
- [17] W. Lauterborn and H. Bolle. Experimental investigations of cavitation-bubble collapse in the neighbourhood of a solid boundary. *Journal of Fluid Mechanics*, 72(2): 391–399, 1975.
- [18] A. Jayaprakash, C. Hsiao, and G. Chahine. Numerical and experimental study of the interaction of a spark-generated bubble and a vertical wall. *Journal of Fluids Engineering*, 134(3):031301, 2012.
- [19] O. Supponen, P. Kobel, D. Obreschkow, and M. Farhat. The inner world of a collapsing bubble. *Physics of Fluids*, 27(9):091113, 2015.
- [20] D. F. de Lange and G. J. de Bruin. Sheet Cavitation and Cloud Cavitation, Re-Entrant Jet and Three-Dimensionality. *Applied scientific research*, 58(1-4):91–114, 1997.
- [21] E. Foeth, T. van Terwisga, and C. van Doorne. On the collapse structure of an attached cavity on a three-dimensional hydrofoil. *Journal of Fluids Engineering*, 130(7):071303, 2008.
- [22] J.K. Jakobsen. On the mechanism of head breakdown in cavitating inducers. *Journal of Basic Engineering*, 86(2):291–305, 1964.
- [23] H. Ganesh, S. A Mäkiharju, and S. Ceccio. Bubbly shock propagation as a mechanism for sheet-to-cloud transition of partial cavities. *Journal of Fluid Mechanics*, 802:37–78, 2016.

-
- [24] O. Coutier-Delgosha, R. Fortes-Patella, and J. Reboud. Evaluation of the turbulence model influence on the numerical simulations of unsteady cavitation. *Journal of Fluids Engineering*, 125(1):38–45, 2003.
- [25] R.E. Bensow and G. Bark. Implicit LES predictions of the cavitating flow on a propeller. *Journal of Fluids Engineering*, 132(4):041302, 2010.
- [26] T. Huuva. *Large eddy simulation of cavitating and non-cavitating flow*. PhD thesis, Chalmers University of Technology, 2008.
- [27] X. Long, H. Cheng, B. Ji, R. Arndt, and X. Peng. Large eddy simulation and Euler–Lagrangian coupling investigation of the transient cavitating turbulent flow around a twisted hydrofoil. *International Journal of Multiphase Flow*, 2017.
- [28] N. Dittakavi, A. Chunekar, and S. Frankel. Large Eddy Simulation of Turbulent-Cavitation Interactions in a Venturi Nozzle. *Journal of Fluids Engineering*, 132(12):121301, 2010.
- [29] B. Huang, Y. Zhao, and G. Wang. Large eddy simulation of turbulent vortex-cavitation interactions in transient sheet/cloud cavitating flows. *Computers and Fluids*, 92:113–124, 2014.
- [30] B. Ji, X. W. Luo, R.E.A. Arndt, X. Peng, and Y. Wu. Large Eddy Simulation and theoretical investigations of the transient cavitating vortical flow structure around a NACA66 hydrofoil. *International Journal of Multiphase Flow*, 68:121–134, 2015.
- [31] N. Lu, R.E. Bensow, and G. Bark. Large eddy simulation of cavitation development on highly skewed propellers. *Journal of Marine Science and Technology*, 19(2): 197–214, 2014.
- [32] A. Asnaghi, A. Feymark and R.E. Bensow. Numerical investigation of the impact of computational resolution on shedding cavity structures. *International Journal of Multiphase Flow*, 2018.
- [33] M. Gavaises, F. Villa, P. Koukouvinis, M. Marengo, and J. Franc. Visualisation and LES simulation of cavitation cloud formation and collapse in an axisymmetric geometry. *International Journal of Multiphase Flow*, 68:14–26, 2015.
- [34] T. Van, P. Fitzsimmons, E. Foeth, and Z. Li. Cavitation erosion: A critical review of physical mechanisms and erosion risk models. In *7th International Symposium on Cavitation, Michigan, USA*, 2009.
- [35] Z. Li, M. Pourquie, and T. van Terwisga. Assessment of cavitation erosion with a urans method. *Journal of Fluids Engineering*, 136(4):041101, 2014.
- [36] R. Fortes-Patella, A. Archer, and C. Flageul. Numerical and experimental investigations on cavitation erosion. In *IOP Conference Series: Earth and Environmental Science*, volume 15, page 022013. IOP Publishing, 2012.
- [37] ZR Li. *Assessment of Cavitation Erosion with a Multiphase Reynolds-Averaged Navier-Stokes Method*. PhD thesis, Delft University of Technology, 2012.
-

- [38] N. Ochiai, Y. Iga, M. Nohmi, and T. Ikohagi. Study of quantitative numerical prediction of cavitation erosion in cavitating flow. *Journal of Fluids Engineering*, 135(1):011302, 2013.
- [39] P. Koukouvini, G. Bergeles, and M. Gavaises. A cavitation aggressiveness index within the Reynolds averaged Navier Stokes methodology for cavitating flows. *Journal of Hydrodynamics*, 27(4):579–586, 2015.
- [40] J. Franc, M. Riondet, A. Karimi, and G.L. Chahine. Impact load measurements in an erosive cavitating flow. *Journal of Fluids Engineering*, 133(12):121301, 2011.
- [41] C. Eskilsson and R. E. Bensow. Estimation of cavitation erosion intensity using CFD: numerical comparison of three different methods. In *Fourth International Symposium on Marine Propulsors, Texas, USA*, 2015.
- [42] M. Mihatsch, S. Schmidt, and N. Adams. Cavitation erosion prediction based on analysis of flow dynamics and impact load spectra. *Physics of Fluids*, 27(10):103302, 2015.
- [43] S. Mottyll and R. Skoda. Numerical 3d flow simulation of ultrasonic horns with attached cavitation structures and assessment of flow aggressiveness and cavitation erosion sensitive wall zones. *Ultrasonics sonochemistry*, 31:570–589, 2016.
- [44] B. Budich, S. Schmidt, and N. Adams. Numerical investigation of a cavitating model propeller including compressible shock wave dynamics. In *Fourth International Symposium on Marine Propulsors, Texas, USA*, 2015.
- [45] B. Budich, S. Schmidt, and N. Adams. Numerical simulation of cavitating ship propeller flow and assessment of erosion aggressiveness. In *Fourth International Symposium on Marine Propulsors, Texas, USA*, 2015.
- [46] W. Pfitsch, S. Gowing, D. Fry, M. Donnelly, and S. Jessup. Development of measurement techniques for studying propeller erosion damage in severe wake fields. In *7th International Symposium on Cavitation, Michigan, USA*, 2009.
- [47] H.G. Weller, G. Tabor, H. Jasak, and C. Fureby. A tensorial approach to computational continuum mechanics using object-oriented techniques. *Computers in physics*, 12(6):620–631, 1998.
- [48] N. Lu, R. E. Bensow, and G. Bark. LES of unsteady cavitation on the delft twisted foil. *Journal of Hydrodynamics, Ser. B*, 22(5):784–791, 2010.
- [49] A. Asnaghi, A. Feymark and R.E. Bensow. Improvement of cavitation mass transfer modeling based on local flow properties. *International Journal of Multiphase Flow*, 93:142–157, 2017.
- [50] J. Sauer. Instationär kavitierende strömungen-ein neues modell, basierend auf front capturing (vof) und blasendynamik. *Diss., Uni Karlsruhe*, 2000.
- [51] L. YuanHui. Equation of state of water and sea water. *Journal of Geophysical Research*, 72(10):2665–2678.

-
- [52] W. Wagner and H. Kretzschmar. *International Steam Tables-Properties of Water and Steam based on the Industrial Formulation IAPWS-IF97: Tables, Algorithms, Diagrams, and CD-ROM Electronic Steam Tables-All of the equations of IAPWS-IF97 including a complete set of supplementary backward equations for fast calculations of heat cycles, boilers, and steam turbines*. Springer Science & Business Media, 2007.
- [53] C. Egerer, S. Hickel, S. Schmidt, and N. Adams. Large-eddy simulation of turbulent cavitating flow in a micro channel. *Physics of Fluids*, 26(8):085102, 2014.
- [54] S. Schmidt. *A low Mach number consistent compressible approach for simulation of cavitating flows*. PhD thesis, Technische Universität München, 2015.
- [55] G. B. Wallis. *One-dimensional two-phase flow*. McGraw-Hill, 1969.
- [56] V. Venkatakrishnan. Convergence to steady state solutions of the Euler equations on unstructured grids with limiters. *Journal of Computational Physics*, 118(1):120–130, 1995.
- [57] A. Gnanaskandan and K. Mahesh. A numerical method to simulate turbulent cavitating flows. *International Journal of Multiphase Flow*, 70:22–34, 2015.
- [58] J.G. Zheng, B.C. Khoo, and Z.M. Hu. Simulation of wave-flow-cavitation interaction using a compressible homogenous flow method. *Communications in Computational Physics*, 14(2):328–354, 2013.
- [59] L Rayleigh. On the pressure developed in a liquid during the collapse of a spherical cavity: Philosophical magazine series 6, 34, 94–98, 1917.
- [60] J. Leroux, O. Coutier-Delgosha, and J. A. Astolfi. A joint experimental and numerical study of mechanisms associated to instability of partial cavitation on two-dimensional hydrofoil. *Physics of Fluids*, 17(5):052101, 2005.
- [61] K. Laberteaux and S. Ceccio. Partial cavity flows. part 1. cavities forming on models without spanwise variation. *Journal of Fluid Mechanics*, 431:1–41, 2001.
- [62] A. Gnanaskandan and K. Mahesh. Large eddy simulation of the transition from sheet to cloud cavitation over a wedge. *International Journal of Multiphase Flow*, 83:86–102, 2016.